

STRUCTURE – FUNCTIONAL RELATIONSHIPS OF RIGHT HANDED
COILED-COIL (RHCC) FROM THE ARCHAEA, *STAPHYLOTHERMUS*
MARINUS

BY

EFEHI KELLY OGBOMO

A Thesis Submitted to the Faculty of Graduate Studies in Partial Fulfilment of
the Requirements for the Degree of

MASTER OF SCIENCE

Faculty of Science
Department of Chemistry
University of Manitoba
Winnipeg, Manitoba, Canada

Copyright © 2010 by Efehi Kelly Ogbomo

ABSTRACT

Proteins from hyperthermophilic microorganisms are characterized by their ability to withstand temperatures in excess of 80°C without loss of function or structure. Due to these properties there is great interest in both the academic and industrial world in understanding how these proteins are capable of retaining their biological activity under such harsh environmental conditions. The purpose of this thesis was to study a 52 amino acid fragment of the tetrabrachion stalk domain from *Staphylothermus marinus*, that is known as Right Handed Coiled Coil (RHCC). This protein is of interest due to its extreme thermostability and its affinity for heavy metals. The aims of this thesis are to better understand the reason for the extreme thermal stability of the protein and to take advantage of the proteins affinity for heavy metals with a view to developing a novel approach to bioremediate Hg^{2+} which is a major environmental pollutant. Our results clearly indicated that the protein is more thermostable in alkaline conditions in comparison to acidic conditions. We believe this observation can be explained by careful inspection of the high resolution structure. Coiled-coil domains are known to be specialized by both the “knobs into holes” (hydrophobic) and salt bridge (ionic) interactions. Under alkaline conditions both these interactions are possible. However, under the acidic conditions tested the aspartic acid and glutamic acid would become protonated and so the salt bridges will no longer be able to form. With regard to the mercury bioremediation experiments, the data clearly show that RHCC is able to bind ionic mercury compounds such as mercury nitrate and dipotassium mercury iodide. In addition, our data from the X-ray diffraction analysis of RHCC – mercury complex show that RHCC protein is able to bind aqueous ionic mercury and localize the mercury in its cavity in a reduced less reactive form Hg^0 .

ACKNOWLEDGEMENT

First and foremost, I would like to give my most heartfelt thanks to my supervisor, Dr Jörg Stetefeld. Over the course of this program, he has inspired me to become a more skillful and knowledgeable researcher. His mentorship and support has been key to the success of my thesis and I am forever grateful for his contribution. A special thank you to Dr George Orriss for proofreading my thesis and providing me with the necessary feedback that has enabled me to successfully complete my work. To Debbie Armstrong for helping me to analyze my mercury samples, your patience and feedback were crucial for the optimization of my mercury experiments.

To Dr Feiyue Wang and Dr Joe O' Neil, thank you for allowing me access to the equipment I needed to complete my research. I am appreciative to Dr Deborah Court, for accepting to be my external examiner. I would like to thank Dr Markus Meier, Dr Simone Karracsh, Dr Trushar Patel, Dr Sivakumar Gajjeraman and Dr Marcos Lemes for being exceptional mentors and role models. To the rest of my lab colleagues: Ainsley, Alex, Laura, Natalie and Mina, it has been a pleasure working with you all in such a fun atmosphere. I wish you all continued success in your work.

Lastly, I would like to recognize and thank my parents and siblings for all of their love and continual support throughout the years, and my best friends Sara Reid and Osamuyi Asemota for their moral support and encouragement.

DEDICATION

To my parents, Chief (Dr) & Mrs S. A. Ogbomo.

TABLE OF CONTENTS

ABSTRACT	i
ACKNOWLEDGEMENT	ii
DEDICATION	iii
TABLE OF CONTENTS	iv
LIST OF TABLES	vii
LIST OF FIGURES	viii
ABBREVIATIONS	x
1. INTRODUCTION	1
1.1 <i>Archaea</i>	2
1.2 <i>Staphylothermus marinus</i>	3
1.3 Coiled-coil motif	6
1.4 Thermostability	9
1.5 Coiled-coil hydrophobic cavity	10
1.6 Bioremediation of mercury	13
2. MATERIALS AND METHODS	14
2.1 DNA Methods	15
2.1.1 Generation of RHCC expression construct	15
2.1.2 Bacterial medium and agar preparation	15
2.1.3 Preparation of competent cells	15
2.1.4 Preparation of RHCC plasmid stock	16
2.1.5 Quantitative determination of plasmid DNA	16
2.1.5.1 Spectrophotometric determination of plasmid concentration	16
2.1.6 Transformation of bacterial cells with plasmid DNA	17
2.2 Protein Expression and Purification	17
2.2.1 Bacterial growth and expression of recombinant right handed coiled-coil protein	17
2.2.2 Lysis of bacterial cells	17
2.2.3 Purification of the Tetrabrachion protein	18
2.2.4 Tricine SDS-PAGE	18
2.2.5 Removal of His ₆ -tag from the purified protein	19
2.2.6 Western Blotting	20
2.2.6.1 Transfer of proteins to Nitrocellulose membranes	20

2.2.6.2	Detection of RHCC protein with the Anti His-Antibody	20
2.2.7	Determination of protein standard concentration	20
2.3	Dynamic Light Scattering (DLS)	21
2.4	Protein X-ray Crystallography	23
2.4.1	Crystallization of RHCC	23
2.4.2	Data collection and processing	23
2.5	Circular dichroism	24
2.5.1	CD Instrument calibration	24
2.5.2	RHCC sample measurements and data processing	25
2.5.3	Spectrum measurements	26
2.5.4	Variable temperature measurement	26
2.6	Bioremediation of Hg ²⁺ ion from aqueous solution	27
2.6.1	Mercury stock preparation	27
2.6.2	Preparation of RHCC	27
2.6.3	Biosorption of Hg ²⁺ ions by RHCC using dialysis method	27
2.6.3.1	Dialysis method	27
2.6.4	Sample collection and storage	28
2.6.5	Mercury Detection Using Cold Vapour Atomic Fluorescence Spectrometry (CVAFS)	29
2.6.5.1	Summary of method	29
2.7	Statistical analysis	30
3.	RESULTS AND DISCUSSION	31
3.1	Purification of the RHCC protein in the cytoplasm of E.coli	32
3.1.2	Proteolysis of Histidine tag	33
3.1.3	Western blotting	34
3.1.4	Determination of the size and homogeneity of RHCC	34
3.2	X-ray Crystallography of native RHCC	37
3.2.1	Crystals and X-ray diffraction	38
3.2.2	Crystal lattice contacts	40
3.2.3	Cavity content	42
3.3	RHCC thermostability based on pH and thermal denaturation	44
3.3.1	RHCC intrahelical and interhelical ionic Interaction	45
3.3.2	Far-UV spectrum and thermal denaturation profile	46
3.3.2.1	RHCC in water pH 7.0	46
3.3.2.2	RHCC in aqueous buffer at pH 10.0	48
3.3.2.3	RHCC in aqueous buffer at pH 2.0	50

3.3.3 Thermal denaturation profile	51
3.4 Bioremediation of Hg ²⁺ ions from aqueous solution	55
3.4.1 Solution analysis using dialysis and CVAFS detection method	57
3.4.1.1 Potassium Mercury Iodide (K ₂ HgI ₄) Analysis	57
3.4.1.2 Mercury Nitrate (Hg(NO ₃) ₂) Analysis	59
3.4.1.3 Determination of the ratio of Hg ²⁺ bound to RHCC	61
3.5 X-ray Crystallography analysis of Hg ²⁺ – RHCC complex	63
3.5.1 Non-thiol binding of Hg insight the hydrophobic cavities of RHCC	63
4. CONCLUSIONS	68
5. REFERENCES	70

LIST OF TABLES

Table 3-1: Data collection and refinement statistics between RHCC at 1.4 Å (spacegroup P3 ₁ 21) and 2.0 Å (spacegroup P2 ₁ 2 ₁ 2 ₁) resolution-both measured using the in-house rotating anode.	39
Table 3-2: Summary of molar ellipticity and percentage change in ellipticity thermal scan signals of RHCC at 222 nm.	53
Table 3-3: Data collection and refinement statistics between RHCC at 1.4 Å (spacegroup P3 ₁ 21), 3.3 Å (spacegroup P2 ₁ 2 ₁ 2 ₁) and 3.15 Å (spacegroup P2 ₁ 2 ₁ 2 ₁) resolution measured in-house and in the Synchrotron.	65

LIST OF FIGURES

Figure 1-1: Diagrammatic representation of tetrabrachion in the S-layer of <i>S. marinus</i>	3
Figure 1-2: Representation of the tetrabrachion and STABLE protease complex of the S-layer of <i>S. marinus</i>	5
Figure 1-3: Right handed coiled coil sequence and its crystal structure	8
Figure 1-4: Crystal structure of the pentameric and tetrameric coiled-coil proteins revealing their hydrophobic cavities	12
Figure 2-1: Sequence of the RHCC construct.	19
Figure 2-2: A simple dialysis setup, showing the control and experiment	28
Figure 3-1: Purification of RHCC by Ni-NTA affinity column	32
Figure 3-2: Proteolytic cleavage of His ₆ -tag from RHCC	33
Figure 3-3: Analysis of Thrombin digested RHCC by Western Blotting	34
Figure 3-4: Size measurement of RHCC by DLS instrument	35
Figure 3-5: Hydrodynamic radii of RHCC obtained at 20 °C in ultrapure water as a function of the protein concentration	36
Figure 3-6: RHCC protein crystals. Crystals grew at 20 °C for one week	38
Figure 3-7: Comparison of crystal contacts between RHCC in spacegroup P212121 with RHCC in spacegroup P3121	41
Figure 3-8: Superposition of the final refined 2DFo-mFc map at 2 Å resolution (1.5σ contour level) onto the crystal structure containing water cluster (Stetefeld 2001, pdb-code 1FE6)	43
Figure 3-9: 1.8 Å resolution electron density map of a fragment of the RHCC tetramer	46
Figure 3-10: Far-UV CD spectra of RHCC in water pH 7.0	47
Figure 3-11: Far-CD spectra of RHCC at pH 10.0	49
Figure 3-12: Far-CD spectra of RHCC at pH 2.0	50
Figure 3-13: Thermal denaturation curves of RHCC measured at 222 nm	52
Figure 3-14: Thermal scan for fraction alpha helicity of RHCC measured at 222 nm	54
Figure 3-15: Uptake of Hg ²⁺ ions by RHCC	58
Figure 3-16: Biosorption of Hg ²⁺ ions from potassium mercury iodide by RHCC	59
Figure 3-17: Effect of Hg ²⁺ ions by RHCC	60
Figure 3-18: Biosorption of Hg ²⁺ ions from mercury nitrate compound by RHCC	61

Figure 3-19: Line plot for the total number of Hg ²⁺ ions bound to RHCC within a week	62
Figure 3-20: Anomalous difference Fourier map for mercury (K ₂ HgI ₄ and Hg(NO ₃) ₂) insight the tetrameric channel of RHCC	64
Figure 3-21: Detailed view of Superposition of the final refined 2DFo-mFc map (blue coloured) at 3.3 Å resolution (1.5 σ contour level) onto the crystal structure containing the Hg from the K ₂ HgI ₄ soak experiment	66
Figure 3-22. Structural changes upon mercury storage	67

ABBREVIATIONS

®	Registered sign
°C	Degree Celsius
µg	Microgram
µl	Microlitre
Å	Angstrom
CAPB	Cocoamidopropylbetaine
cm	Centimetre
DLS	Dynamic Light Scattering
DNA	Deoxyribonucleic acid
ECL	Enhanced chemiluminescent
ECM	Extracellular Matrix
EDTA	Ethylene Diamine Tetraacetic Acid
HRP	Horseradish peroxidase
kDa	Kilodalton
ml	Millilitre
mm	Millimeter
mM	Millimolar
nm	Nanometer
Ni-NTA	Nickel-nitrilotriacetic acid
OD	Optical Density
PDB	Protein Database
SDS-PAGE	Sodium Dodecyl Sulfate Polyacrylamide Gel Electrophoresis
S-layer	Surface layer
RHCC	Right-handed Coiled-coil

1. INTRODUCTION

1.1 *Archaea*

Archaea are simple single celled microorganisms that contain neither a cell nucleus nor the other organelles found in higher organisms. They are known to come from 'specialized' or 'extreme' habitats like hot acidic niches (thermoacidophiles), highly concentrated salt environments (halophiles), sulfur-rich (*sulfolobus*) and redox environments (methanogens), (Woese *et al.*, 1978). More recently, *Archaea* have been found to exist in less harsh habitats such as soils, oceans and marshlands. *Archaea* are of great interest due to their involvement in the carbon and nitrogen cycles (Woese *et al.*, 1977). *Archaea* have a similar cell structure as bacteria, although there are important differences in the composition and organization between them (Woese *et al.*, 1978). Overall, their make-up most closely resembles that of gram positive bacteria in that they possess a plasma membrane and a cell wall, but lack a periplasmic space. Most *Archaea* possess unusual protein structures and properties on the surface of their cell wall. Of interest to this study is the *Staphylothermus marinus*, which possesses a filiform glycoprotein complex tetrabrachion that forms the surface (S-) layer of the organism (Fig.1-1) (Mayr *et al.*, 1996). The S-layer forms a rigid assembly of protein molecules that coat the outside of the cell, thus affording the cell membrane protection against potentially damaging solutes and macromolecules.

As a consequence of their biotopic adaptations, *Archaea* can mostly grow optimally at high temperatures (> 80 °C), can tolerate a wide range of pH (2-10), high redox potential, pressure and salinity (Mayr *et al.*, 1996). Enzymes and other proteins isolated from these organisms share this ability to withstand the extreme conditions. Studies of hyperthermophiles have provided information in regard to molecular evolution, the diversity of metabolism, and the nature of protein stability. Due to the fact that many enzymes of hyperthermophilic microorganisms have a capacity to operate at high temperatures, researchers have looked for a

biotechnological application that takes advantage of this property. However, to date only a limited number of high-resolution crystal structures are available for hyperthermophilic enzymes (Byum *et al.*, 2007; Rhee *et al.*, 2006; Vonrhein *et al.*, 1998; Singleton *et al.*, 1999; Kirino *et al.*, 1994; Kelly *et al.*, 1993) and so, it is hard to draw any conclusions as to why these proteins are so thermostable.

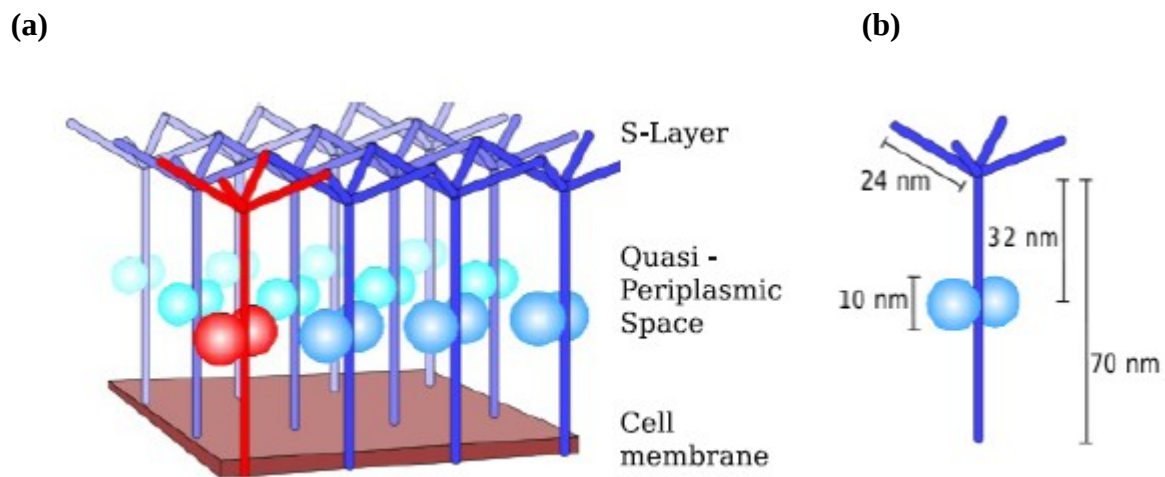


Figure 1-1: Diagrammatic representation of tetrabrachion in the S-layer of *S. marinus*.

(a) Canopy-like arrangement of the tetrabrachion stalk anchored to the *S. marinus* cell membrane. (b) Dimensions of the tetrabrachion stalk. The spherical balls represent the STABLE protease that is used for peptide-fermentation in *S. marinus* (Mayr *et al.*, 1996, for copyright permission please go to http://s100.copyright.com/CustomerAdmin/PLF.jsp?IID=2010081_128267767).

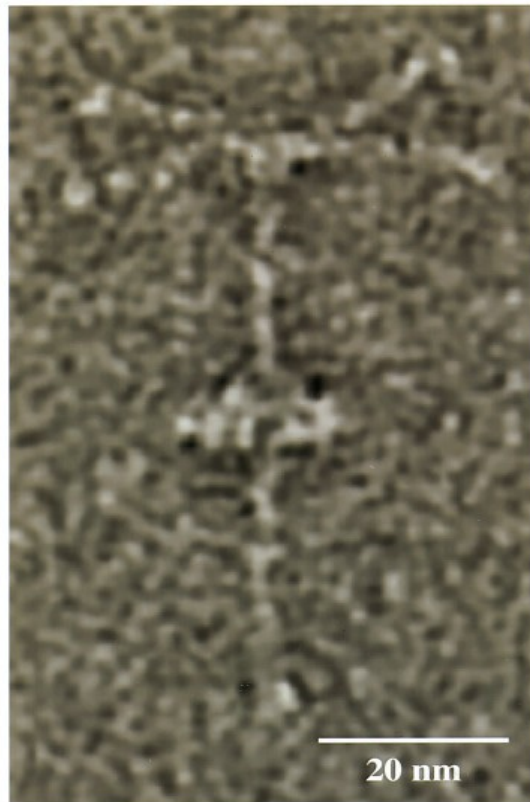
1.2 *Staphylothermus marinus*

Staphylothermus marinus is a hyperthermophilic archaeobacterium that was first isolated from a geothermally-heated marine environment (Fiala *et al.*, 1986). It is a strict anaerobe that is capable of oxidizing elemental sulphur and has an optimum growth

temperature of 92 °C. In addition, it possesses a peptide-fermenting activity. *S. marinus* is no different from other *Archaea*, in that its cell membrane is covered by an S-layer. In contrast to the highly ordered crystalline S-layers of *Thermoproteus tenax* (Wildhaber & Baumeister, 1987) and *Pyrobaculum organotrophum* (Phipps *et al.*,1991), the S-layer formed by *S. marinus* is a poorly ordered network that in some respect resembles the subunits of some Extracellular Matrix (ECM) proteins of eukaryotes (Engel & Furthmayr, 1987). The scaffold for the S-layer of *S. marinus* is formed by an extended filiform glycoprotein complex called tetrabrachion. Tetrabrachion comprises an α -helical stalk of 70 nm in length that is anchored to the cell membrane at its C-terminal end, and an N-terminal domain consisting of four arms each approximately 24 nm in length. In contrast to the α -helical stalk, the secondary structure of the N terminal domain is predicted to be formed entirely of β -strands. The arms of the N-terminal domain form end to end contacts with the canopy-like meshwork of the *S. marinus* S-layer and give rise to a “quasi-periplasmic space”.

The tetrabrachion complex is made up of two polypeptide chains termed the “heavy” and “light” chain with molecular weights of 92 kDa and 85 kDa, respectively. Four copies of the heavy chain associate with each other to form a parallel four stranded α -helical coiled coil that is membrane anchored. At the top of the coiled coil portion, there is a hinge domain that results into the divergence of the four strands from each other (Fig.1-2). At this point, the N terminal parts of the “heavy” chain associate with the “light” chain to give rise to the four arms of tetrabrachion. Approximately 32 nm from the “hinge” region, two globular particles of 10 nm in diameter were observed by electron microscopy (Fig.1-2a). The globular particles were shown to exhibit tryptic and chymotryptic protease activity which has since been assigned to the protease known as STABLE (stalk-associated archaeobacteria endo-protease. (Mayr *et al.*, 1996; Peters *et al.*, 1996).

(a)



(b)

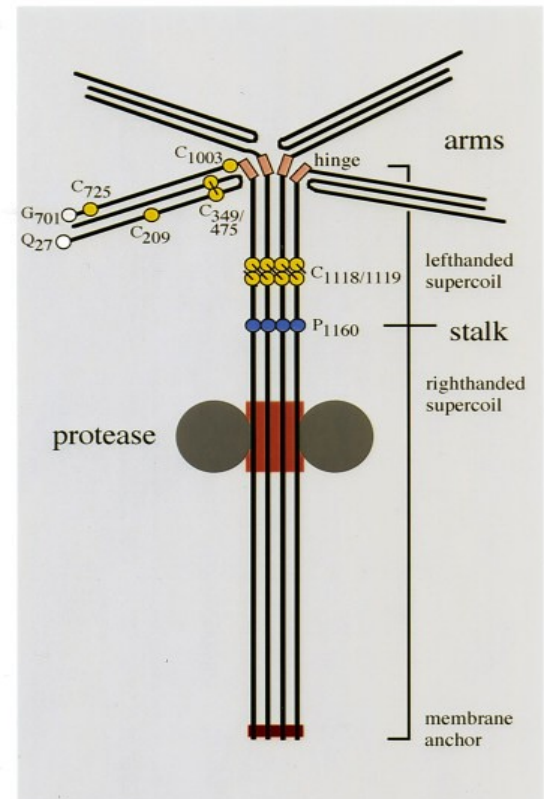


Figure 1-2: Representation of the tetrabrachion and STABLE protease complex of the S-layer of *S. marinus*. (a) Electron micrograph of a single complex specimen (left). (b) Schematic illustration of the proposed basic folding topology (right). The key proline and cysteine residues are shown in blue and gold, respectively. The scaffold which binds to the STABLE protease is shown in the red rectangle and forms a small part of the stalk, which is membrane anchored (Peters *et al.*, 1996, http://s100.copyright.com/CustomerAdmin/PLF.jsp?IID=2010081_1282678398507)

Interestingly, whilst the 70 nm stalk forms a tetrameric coiled-coil bundle, the properties of the S-layer stalk are not uniform throughout its length. For example, the first 130 amino acid residues after the hinge up until the key residue Pro 1160, show a classical heptad repeat motif that is characteristic of “left handed coiled-coils”. However, after Pro1160, the

heptad repeat is replaced by an undecad repeat that results in the formation of a right-handed coiled-coil structure. It is on the right handed part of the “stalk” that the STABLE protease binds to. A major feature of the tetrabrachion stalk domain is its extreme thermostability even in the presence of 1 % (w/v) sodium dodecyl sulfate (SDS), 6M guanidine, or 70 % (w/v) sulfuric acid (Mayr *et al.*, 1996). These features make the tetrabrachion an interesting model system to understand the factors governing the thermal stability of coiled coils.

1.3 Coiled-coil motif

The coiled coil is the most common oligomerization motif found in proteins (Cohen & Parry, 1990; Peter *et al.*, 1996; Kohn *et al.*, 1997). A characteristic of this type of motif is the presence of a heptad repeat $(abcdefg)_n$ which is observed in one tenth of the proteins deposited in the protein database (PDB) (Walshaw & Woolfson, 2001). Based on repeat patterns obtained by Perutz and coworkers for tropomyosin and other related fibrous proteins (Perutz *et al.*, 1951), Crick was able to predict in the early 1950's that such repeat could only be possible due to the interlocking of at least two α -helices in a specialized motif that repeats itself every 7 residues or 2 helical turns (Crick, 1952; 1953a,b). Crick predicted that this motif would produce an α -helix with 3.5 residues per turn compared to the conventional 3.6 seen in an undistorted α -helix. An interesting property of a coiled-coil is that it generates an amphipatic helix with an hydrophobic core at positions 'a' and 'd' in the repeat and polar residues on the outer face. This hydrophobic interaction gave birth to the famous “knobs-into-holes” arrangement and was first proposed by Crick (Crick, 1952; 1953). Crick's approach described the packing of amino acids between adjacent α -helices and was shown to be correct with the structure of the glycoprotein from influenza virus (Wilson *et al.*, 1981).

Furthermore, there is the 4,3-spacing that is common to all coiled-coil motifs that

display a heptad repeat. This spacing permits all the core hydrophobic residues to be on the same side of the helix thereby facilitating the “knobs-into-holes” packing. Coiled-coil motifs can be oligomers e.g dimers, trimers, tetramers, pentamers and heptamers (O'Shea *et al.*, 1991; DeLano *et al.*, 1994; Efimov *et al.*, 1996; Malashkevich *et al.*, 1996; Liu *et al.*, 2006). Helices that originate from the same protein chain are referred to as homo-oligomers and helices that originate from different protein chains are designated hetero-oligomers.

The handedness of a standard α -helix is right-handed (Ramachandran *et al.*, 1963). However, in coiled-coil domains the helix becomes supercoiled and so it adopts the opposite handedness to the helix which formed it (Pauling *et al.*, 1951). Pauling recognized that in addition to the classical 7/2 repeat, coiled coils could also result from 11/3, 15/4, 18/5 and 25/7 repeats. Interestingly and pertinent to this thesis, Pauling predicted that 7/2 and 15/4 repeats would generate supercoiled helices of opposite handedness and so coiled-coil domains could either be left-handed or right-handed. Protein sequences and structures with an undecad (Peters *et al.*, 1996; Stetefeld *et al.*, 2000), pentadecad (Kühnel *et al.*, 2004; Hoiczky *et al.*, 2000; Noreen *et al.*, 1999) and 25 residue repeat (Tarbouriech *et al.*, 2000) have since been supported.

Of interest to this research is a 52 residue short tetrameric bundled protein called Right handed coiled-coil (RHCC) which corresponds to the part of the tetrabrachion stalk that binds to the STABLE protease. The RHCC polypeptide chain fragment forms a parallel right handed coiled coil with an average length and width of 72 Å and 25 Å respectively. It has a 11/3 residue repeat, with the N-terminal part more supercoiled than the C-terminal part due to the presence of a stutter between Ile11 and Thr16 (Fig.1-3) (Stetefeld *et al.*, 2000). More interestingly is the unique 7,4 residue repeat which is different from the predicted 4,4,3 repeat as found in an artificially produced right handed coiled coil (Harbury *et al.*, 1998).

a

	a	b	c	d	e	f	g	h	i	j	k
1-3									G	S	I
4-11	I	N	E	T	A	D	D	I			
12-18					V	Y	R	L	T	V	I
19-29	I	D	D	R	Y	E	S	L	K	N	L
30-40	I	T	L	R	A	D	R	L	E	M	I
41-51	I	N	D	N	V	S	T	I	L	A	S
52	I										

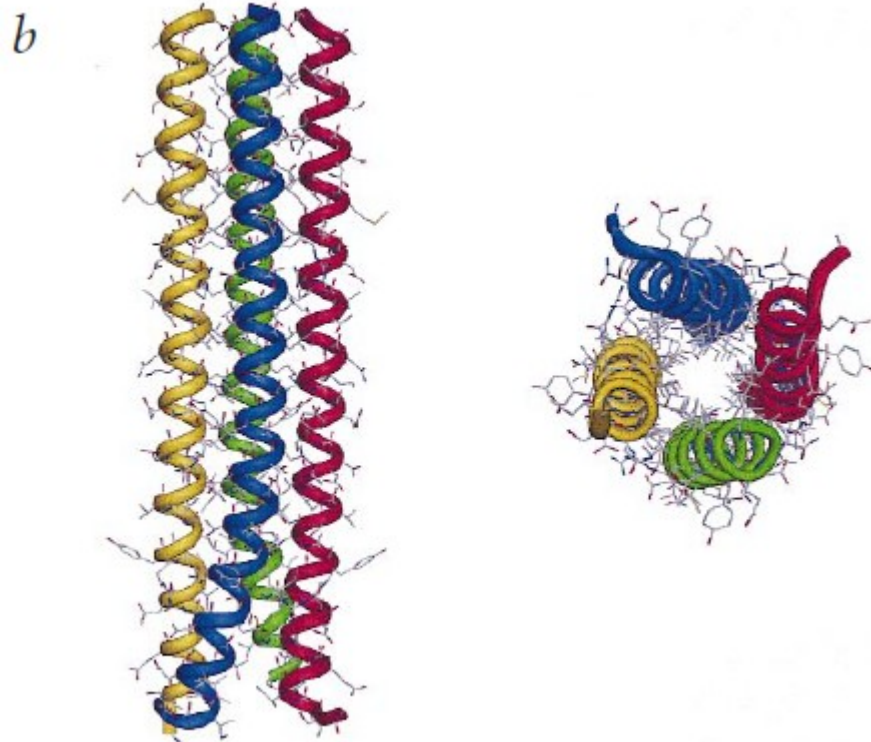


Figure 1-3: Right handed coiled coil sequence and its crystal structure. “(a) The 52 amino acid residues of RHCC are shown with the 7,4 residue repeat positions indicated by the residues labelled in RED. (b) Side view (left) of RHCC at 1.8 Å resolution, the four helices of the coiled-coil are shown in red, blue, yellow and green, respectively. The N-terminus is at the bottom, and the C-terminus is at the top of the figure. Axial view (right) from the N-terminus of RHCC” (Stetefeld *et al.*, 2000, http://s100.copyright.com/CustomerAdmin/PLF.jsp?IID=2010081_1282680223491).

1.4 Thermostability

Over the years, we have seen that proteins originating from thermophilic and hyperthermophilic organisms have an intrinsic capability to survive at temperatures significantly higher than physiological temperatures. Hyperthermophilic microorganisms have consistently been of interest to scientists from various disciplines and this interest has rapidly increased within the past two decades. Thermophilic proteins are of interest to those studying the molecular mechanisms of protein stability, thermotolerance, and in the industrial sector for those who are looking to use enzymes as biocatalysts with longer shelf-lives (Chou *et al.*, 2008; Scandurra *et al.*, 1998). Protein adaptation to extreme temperature requires an optimization of the internal non-covalent as well as protein solvent interactions (Ladenstein and Antranikian, 1998). However, the key question of why certain proteins are more thermostable than others has not been answered and this is the driving force for our research.

Ladenstein and Antranikian proposed that the thermostability of folded proteins, results from a delicate balance between van der Waals forces, hydrogen bonding, charge-charge interactions (e.g salt bridges) and hydrophobic effects. Furthermore, these interactions increase the amount of buried hydrophobic residues and maximize the formation of salt bridges. This encourages favourable interactions and decrease the ratio of surface area to volume (Stellwagen *et al.*, 1978).

In relation to coiled coils, the “knobs-into-holes” packing described by Crick is a key feature that provides stability for coiled-coil motifs. The stability of the coiled coil is achieved by the systematic packing and interaction of amino acids side chains in the 'a' and 'd' positions along the hydrophobic face of the motif (Tripet *et al.*, 2000; Wagschal *et al.*, 1999). The RHCC protein from *S. marinus* has “knobs-into-holes” interaction between helices. The side chains at position 'a' and 'h' of the undecad repeats of RHCC interact hydrophobically like the

'a' and 'd' interaction found in left handed coiled coils (Stetefeld *et al.*, 2000; McFarlane *et al.*, 2009). Despite the simplicity of the coiled-coil arrangement, such proteins are typically more thermostable than proteins lacking a coiled-coil motif. There have been reports that the hydrophobic interaction in coiled coils may be the main driving force for coiled coil stability (Munson *et al.*, 1996). Munson and coworkers, showed that repacking the core with exclusively hydrophobic Ala₂Leu₂ layers increased coiled coil stability.

However, interhelical salt bridges have also been shown to contribute to thermostability of the coiled-coil motifs (Lavigne *et al.*, 1996; McClain *et al.*, 2002; Meier *et al.*, 2002; 2010). Additional stability can be achieved depending on the length of coiled-coil motif (Litowski *et al.*, 2001). Litowski showed that an increase in the length of a *de novo* designed homodimeric coiled-coil correlates with a non-linear increase in its stability. This result supports a similar effect that was found in four stranded coiled-coils (Fairman *et al.*, 1995). In addition, reports show that the minimum length for the formation of a stable coiled-coil is a three heptad repeat, or 21 residues (Su *et al.*, 1994; Fairman *et al.*, 1995; Lumb *et al.*, 1994).

1.5 Coiled-coil hydrophobic cavity

The presence of cavities in fully folded coiled-coil domains is extremely unusual. Most cavities that have been reported in the literature are hydrophobic and appear typically empty (Matthews *et al.*, 2009). In specialized cases, researchers have shown that some non-polar coiled coil cavities surprisingly contain water molecules (Malashkevich *et al.*, 1996; Stetefeld, *et al.*, 2000), which is in contrast with polar cavities that readily accommodate water molecules (Rashin *et al.*, 1986; Williams *et al.*, 1994; Buckle *et al.*, 1996). In the past decade, reports have suggested that these hydrophobic cavities introduce an additional degree of

stability (Stetefeld *et al.*, 2000; Liu *et al.*, 2009) for such proteins, due to hydrophobic interactions. In addition, there are reports in the literature showing that some internal cavities are capable of binding heavy atom derivatives (Stetefeld *et al.*, 2000), vitamin A and D₃ (Özbek *et al.*, 2002), retinol (Gonzalez-Fernandez *et al.*, 2009), Cis-platin (Eriksson *et al.*, 2009), and Organic ligands (Mizuno *et al.*, 2009; Gonzalez *et al.*, 1996).

However, large cavities in coiled coil proteins have only been identified in two proteins; the left handed pentameric Cartilage Oligomerization Matrix Protein (COMPcc) (Malashkevich *et al.*, 1996; Efimov *et al.*, 1996) and the tetrameric Right Handed Coiled Coil (RHCC) protein (Stetefeld *et al.*, 2000). Smaller cavities are also present in the right-handed coiled coil of vasodilator-stimulated phosphoprotein (VASP) (Kuhnel *et al.*, 2004). The high stability of coiled coils and the presence of large internal cavities has created a novel approach to drug design and delivery (Eriksson *et al.*, 2009; McFarlane *et al.*, 2009). The pentameric COMPcc contains a 73 Å long axial pore with a diameter of between 2 Å and 6 Å along its length (Fig. 1-4). The COMPcc pore is divided into two large cavities by a ring of conserved Glutamine residues at position 54. Dependent upon the ligand either one or both cavities are filled. The RHCC molecule contains four large globular cavities along the inside of the tetramer (Fig. 1-4), which have sizes in the range 150 Å to 340 Å. These cavities have been shown to bind either heavy metals (Stetefeld *et al.*, 2000) used for structure solution or to the anti-cancer drug, Cis-platin (Eriksson *et al.*, 2009). In the current study, we have investigated the capacity of RHCC to bind a large number of diverse mercury compounds with a view to using it as a possible biological mercury detoxifier.

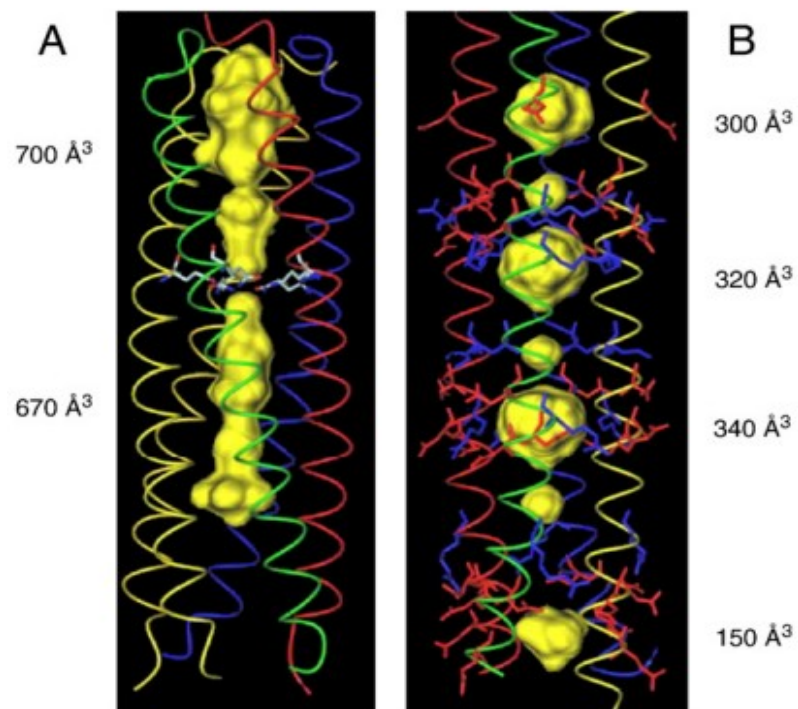


Figure 1-4: Crystal structure of the pentameric and tetrameric coiled-coil proteins revealing their hydrophobic cavities. (A) COMPcc protein with elongated cavities. (B) RHCC protein with globular hydrophobic cavities. Both types of cavities can carry structurally different type of compounds. (McFarlane *et al.*, 2009).

http://s100.copyright.com/CustomerAdmin/PLF.jsp?IID=2010081_1282679793100

1.6 Bioremediation of mercury

Over the years, mercury (Hg) has been identified as a global pollutant due to its toxicity. This toxicity arises due to the strong affinity of the Hg^{2+} ions for the thiol groups (-SH) of proteins. As a result of this reaction, mercury is readily accumulated in biological matter in the surrounding environment. At the current time bioremediation of areas polluted by mercury is extremely difficult as it is far from trivial to convert mercury waste to less toxic compounds that can be more readily disposed of (Okino *et al.*, 2000). Over the past few years a number of different approaches have been adopted with varying degrees of success. One approach has been to use mercury resistant bacteria to reduce Hg^{2+} to HgO (Hansen *et al.*, 1984) while another uses Zinc (Zn) cementation (Ku *et al.*, 2002) to remove mercury from an aqueous environment. A more common approach has been the use of organic and inorganic absorbents to extract mercury from waste waters. A final method worthy of mention is the use of biopolymers to treat mercury waste (Kostal *et al.*, 2003). However, a major limitation in the use of chemical treatments to remove mercury from sites of contamination is that they generate secondary pollution which may be more detrimental than that caused by the mercury (Okino *et al.*, 2000). Therefore, there is much interest in the field in identifying new approaches that remove the damaging mercury ions from the environment without generating any potentially harmful secondary pollution.

2. Material and Methods

2.1 DNA Methods

2.1.1 Generation of RHCC expression construct

The 52 residue coiled-coil domain of Tetrabrachion from *Staphylothermus marinus* was cloned into the vector pET15b at the BamH1 and EcoR1 restriction sites as described in the manual (Novagen) to form the construct pET15b-RHCC. The vector encodes an N-terminal His₆-tag to aid in the purification of RHCC by affinity chromatography (Porath *et al.*, 1975) and a thrombin cleavage site that enables the cleavage of the His-tag residue after purification. Expression of the target protein is under the control of the T7 promoter which is IPTG inducible. The gene that encodes for the antibiotic resistance for the plasmid is ampicillin.

2.1.2 Bacterial medium and agar preparation

Luria Bertani (LB) broth was prepared by dissolving 25 g of LB mix (Research Products International Corporation) into 1 L of milli-Q water. LB/Agar was made by adding 1.5 g of agar per 100 ml of LB. The LB and LB/Agar were sterilized by autoclaving at 121 °C for 30 minutes.

2.1.3 Preparation of competent cells

Cells of *E.coli* strain BL21 (DE3) were grown aerobically in 50 ml of 2 x LB media at 37 °C until an optical density (OD) of 0.6 at 600 nm was obtained. The cells were harvested by centrifugation at 2,200 x g for 10 min at 4°C. The pellet was resuspended in cold 0.1 M calcium chloride (20 ml) and kept on ice for 30 min. The cells were again centrifuged at 2,200 x g for 10 min at 4°C. The competent cells were resuspended in 0.1 M calcium chloride (4 ml) and stored at 4°C. They remained competent for up to 4 days.

2.1.4 Preparation of RHCC plasmid stock

A 1 µl aliquot of a preexisting 100 µg/ml pET15b-RHCC plasmid stock was added to 100 µl of calcium chloride competent DH5α cells. The plasmid was incubated with the cells on ice for 30 minutes. Then the mixture was incubated for 90 seconds at 42 °C (heat shock) before placing back on ice for another 30 seconds. After the heat shock step, 800 µl of LB broth was added to the plasmid /cell mixture before incubating for 2 hours at 37 °C. The mixture was pelleted in a micro-centrifuge at 4,000 x g for 1 minute to remove the excess LB. The pellet was resuspended in the residual LB, with the transformation plated out onto LB/Amp plates and incubated overnight at 37 °C.

A single colony of pET15b-RHCC transformed into DH5α was picked and transferred into 5 ml LB/Amp. The plasmid-containing cells was grown up over night at 37 °C before purification of the plasmid DNA according to the Qiagen mini-prep protocol (Qiagen, U.S.A.). The freshly prepared pET15b-RHCC plasmid stock was stored at -20 °C.

2.1.5 Quantitative determination of plasmid DNA

2.1.5.1 Spectrophotometric determination of plasmid concentration

The plasmid DNA concentration was determined by measuring the absorbance at 260 nm (A_{260}) using a 10-mm quartz cuvette. The concentration was calculated based on the formula (below), where the absorbance of 1 corresponds to 50 µg/ml of DNA (Biochrom Spectrophotometric DNA calculation manual).

$$[\text{plasmid DNA } (\mu\text{g/ml})] = (A_{260}) \times 50 \mu\text{g/ml} \times (\text{DF}) \quad (\text{Eqn. 2.1})$$

where A_{260} is the plasmid absorbance at 260 nm and DF is the dilution factor.

2.1.6 Transformation of bacterial cells with plasmid DNA.

Competent cells (50 μ l) were added to the plasmid DNA (1 μ l), and the mixture was kept on ice for 30 minutes. Then the cells were heated to 42 °C for 90 seconds before placing back on ice. After the heat shock, 100 μ l LB broth was added to the cells and incubated at 37 °C for 30 minutes. The transformed cells were plated out onto LB plates containing 100 μ g/ml ampicillin and incubated overnight at 37 °C.

2.2 Expression and purification of the RHCC

2.2.1 Bacterial growth and expression of recombinant RHCC protein

E.coli cells of strain BL21(DE3) (Studier *et al.*, 1990) were transformed with plasmid DNA, as described above. Precultures were grown by inoculating 50 ml of LB/Amp media with a single colony of BL21/(DE3) transformed with pET15b-RHCC and incubated at 37 °C overnight in a shaker (200 rpm). To 1.6 L of fresh LB/Amp media, 20 ml of preculture was added and the cells were allowed to grow to an OD₆₀₀ of 0.6 at 37 °C with shaking. The cells were induced adding by Isopropyl β -D-1-thiogalactopyranoside (IPTG) to a final concentration of 1 mM. Bacteria cell cultures were kept in the shaker and left to express the RHCC protein for 3 hours. Then the cells were harvested by centrifugation at 6,000 x g for 20 minutes at 4 °C. The LB supernatant was discarded and cell pellets were stored at -20 °C.

2.2.2 Lysis of bacterial cells

The bacterial cell pellet from the 1.6 L expression culture was resuspended in 30 ml Binding buffer [20 mM Tris – Cl, pH 7.5, 5 mM Imidazole, 500 mM NaCl, 8 M Urea] and kept on ice. The cells were lysed by three passages through a French Pressure Cell (SLM Instruments, Urbana IL, U.S.A.). Unlysed cells and cell debris were removed by centrifugation

using a Beckman JA 25.50 rotor (Beckman-Coulter Centrifuge, U.S.A.) at 20,000 x g for 20 minutes at 4 °C.

2.2.3 Purification of the RHCC protein

The purification of His-tagged RHCC was performed at room temperature by affinity chromatography on Ni²⁺-Sepharose (GE Healthcare) under denaturing conditions as described previously (Stetefeld *et al.*, 2000).

2.2.4 Tricine SDS-PAGE

Crude extracts of bacterially expressed proteins, purified proteins and fractions from chromatography columns were analyzed on a Tricine SDS-PAGE gel (Schägger *et al.*, 1987). Protein gels were prepared in mini-gel format (0.07 x 14 x 14 cm) consisting of a 16 %T (w/v) separating gel, 10 %T spacing gel and a 4 %T stacking gel (Schägger *et al.*, 2006). The separating and stacking gels were prepared in buffers containing 3 M Tris-HCl, pH 8.45 and 0.3 % (w/v) SDS. The running buffer consists of an anode buffer (0.2 M Tris-HCl, pH 8.9) and cathode buffer (0.1 M Tris-HCl, 0.1M Tricine, pH 8.25, 0.1% SDS) (Schägger *et al.*, 1987). Gels contained either 10 or 15 wells for samples consisting of 5 - 40 µg protein for optimum resolution.

Protein samples to be run on Tricine SDS-PAGE were prepared by adding an equal volume of loading buffer [0.3 M Tris-HCl, pH 6.8, 10 % (w/v) SDS, 25 % (v/v) glycerol, 5 mM β-mecarptoethanol and 0.015 % (w/v) bromophenol blue] in a 1:1 mixture prior to gel loading. Gels were run at 150 V in a vertical BIO-RAD mini-protein II electrophoresis system. Gels were stained for 90 minutes in Gel Stain [50 % (v/v) methanol, 8 % (v/v) acetic acid , 0.2 % (w/v) Page Blue 83] before destaining in a solution containing 20 % (v/v) methanol, 8

% (v/v) acetic acid.

2.2.5 Removal of His₆-tag from the purified RHCC protein

Removal of the His tag from the purified protein was achieved by using biotinylated thrombin, according to the manufacturer's instruction (EMD Biosciences Inc.) This is possible as the pET15b vector encodes a thrombin cleavage site between the His₆-tag and the N-terminus of the expressed protein (Fig. 2-1). Aliquots of the protein sample was incubated for 2, 4, 8 and 16 hours at room temperature (RT) to identify the optimal cleavage conditions. The cleavage reaction was stopped by a 10 minutes incubation of the reaction mix at 90 °C in a water bath.

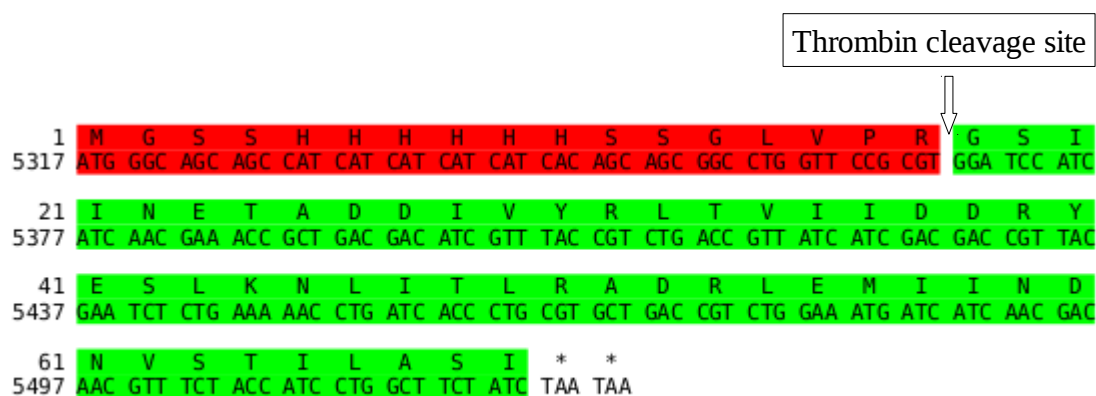


Figure 2-1: Sequence of the RHCC construct. RHCC amino acid residues and codons (green). The start codon (ATG), six Histidines and a section of the cleavage site of the thrombin protease are shown in red. The space separating both colours designate the point cleaving occurs. TAA(*) is a STOP codon.

After the heat inactivation step, the biotinylated thrombin was removed from the sample by passing the thrombin/RHCC mixture over a streptavidin agarose column according to the manufacturer's protocol (EMD Biosciences Inc.). To ensure the complete removal of the

thrombin from the sample, 32 μ l of streptavidin slurry was required per unit of the thrombin protease used. The RHCC with the His₆-tag removed was then dialyzed into the desired buffer.

2.2.6 Western Blotting

2.2.6.1 Transfer of proteins to nitrocellulose membranes

Proteins were transferred from the SDS-PAGE gel onto a nitrocellulose membranes using a Bio-Rad semi-dry blotting apparatus (Bio-Rad Laboratories, Inc. California, U.S.A.). When the Tricine SDS-PAGE gel was ready, it was transferred into Semi dry blot buffer (48 mM Tris-HCl, pH 8.3, 39 mM Glycine, 0.037 % SDS, 20 % methanol) for 10 minutes. Then it was placed into the blotting device in the order: blotting pad, nitrocellulose membrane, gel, blotting pad to form a blotting sandwich. Air bubbles were removed by gently rolling over the sandwich with a 10 ml pipette. The transfer was performed at 105 mA for 45 minutes.

2.2.6.2 Detection of RHCC protein with the anti His-Antibody

The nitrocellulose membrane was placed into a Blocking Buffer (1 X phosphate buffered saline, 0.1 % Tween-20 and 5 % Coffee Whitener) and incubated for 45 - 60 minutes at room temperature. The membrane was washed 3 times with PBS-T (PBS, 0.1 % Tween-20) before adding the Penta-His Horseradish Peroxidase (HRP) antibody (Qiagen Inc – U.S.A.) at a dilution of 1 in 10,000 in Blocking Buffer. The membrane was incubated with the antibody for 45-60 minutes. Then the nitrocellulose membrane was washed with PBS-T as before. The blot was developed using the ECL kit and X-ray film (GE Healthcare, U.S.A.).

2.2.7 Determination of protein standard concentration

Protein samples were dialyzed against ultra pure water and lyophilized using the freeze

mobile method at -50 °C under vacuum as described (Vertis Company Inc Gardener, NY). Lyophilized proteins were accurately weighed into dram vials and dissolved in a certain volume of the required buffer in order to obtain a standard concentration. Alternatively, we measured the absorbance of protein at 280 nm (A_{280}) and 700 nm (A_{700}), with the protein concentration calculated using the equation below.

$$[\text{RHCC (mg/ml)}] = [(A_{280} - A_{700}) * M_{\text{wRHCC}} / \epsilon] \quad (\text{Eqn. 2.2})$$

where M_{wRHCC} is the molecular weight of RHCC monomer which is 5893.7 g/mol, and ϵ is the extinction coefficient for RHCC that has the value 2897.7 $\text{M}^{-1}\text{cm}^{-1}$.

2.3 Dynamic Light Scattering (DLS):

Dynamic light scattering (DLS) measurements were made using Malvern Zetasizer NanoS instrument (Malvern Instruments Ltd) with a He-Ne laser providing a 690 nm light and an output power in the range of 10-50 megawatts. Measurements were performed with protein solutions in 10 mM sodium phosphate buffer, pH = 7.5, at a constant temperature of 20 °C. All samples analyzed were filtered through a 0.1 μm centrifugal filter (Millipore) prior to measurement.

The hydrodynamic parameters for RHCC were determined as follows: the measured translation diffusion coefficient D_T is related to the frictional coefficient f by the Einstein-Sutherland equation:

$$D_T = k_B T / f (\text{cm}^2/\text{s}) \quad (\text{Eqn. 2.3})$$

where k_B is the Boltzmann constant, $1.381 \times 10^{-23} \text{ JK}^{-1}$ and T is the temperature in Kelvin (K).

The frictional coefficient of a spherical particle (f_{sph}) is a function of the fluid viscosity (η) and the radius of the particle (r_{sph}). It is defined by the Stokes law:

$$f_{\text{sph}} = 6\pi\eta r_{\text{sph}} \quad (\text{Eqn. 2.4})$$

The shape of RHCC were characterized using the so-called shape factor F which is informative about the shape of the molecule. This factor represents the ratio between the measured frictional coefficient (f) and the frictional coefficient (f^{theo}) of a hypothetical sphere for which a hypothetical radius is calculated using the molecular mass:

$$F = f / f^{\text{theo}} \quad (\text{Eqn. 2.5})$$

It can be shown that

$$f / f^{\text{theo}} = R_{\text{H}} / R_{\text{H}}^{\text{theo}} \quad (\text{Eqn. 2.6})$$

where R_{H} is the measured hydrodynamic radius, and $R_{\text{H}}^{\text{theo}}$ is the radius of the hypothetical sphere, calculated from the molecular mass. The theoretical hydrodynamic radius was calculated from the formula:

$$R_{\text{H}}^{\text{theo}} = [3M(\bar{v} + h) / (4\pi N_{\text{A}})]^{1/3} \quad (\text{Eqn. 2.7})$$

where M is the molecular mass, \bar{v} is the partial specific volume, h is the hydration, and N_{A} is the Avogadro constant.

The molecular mass of the RHCC tetramer used is 23,574.8 g/mol. \bar{v} has values between 0.69 and 0.75 cm³g⁻¹ for proteins containing only amino acid residues (Cantor and Schimmel, 1980). A value of 0.709 cm³g⁻¹ was used for RHCC (Laue *et al.*, 1992). According to Cantor and Schimmel, hydrations between 0.3 and 0.4 g H₂O (g-protein)⁻¹ are needed to account for the hydrodynamic behaviour of globular proteins. We used a value of 0.40 g H₂O (g-protein)⁻¹.

2.4 Protein X-ray Crystallography

2.4.1 Crystallization of RHCC

RHCC was expressed in *E.coli* and purified as described (Stetefeld *et al.*, 2000). Crystallization experiments were performed at 20 °C by the vapour diffusion method. The drop was prepared by adding 2 µl of pure protein at 13 mg/ml to 2 µl of reservoir solution on a siliconized glass coverslide. The coverslide was placed above 500 µl of the reservoir solution and sealed with silicon grease. The reservoir solution contained 200 mM ammonium acetate, 200 mM Tris-HCl (pH 8.5) and 26 – 30 % of Isopropanol with crystals large enough for X-ray diffraction experiments obtained after 7 days. Crystals were harvested into a cryo-solution containing ethylene glycol and reservoir in a ratio 7:3 (v/v), respectively, before flash freezing in liquid nitrogen and mounting onto a goniometer head. Protein samples were co-crystallized with mercury compounds at 20 °C, performing a set of dilution series of K_2HgI_4 and $Hg(NO_3)_2$ in the range of 0.5-1 mM. A 100 mM stock solution of both mercury nitrate and dipotassium mercury iodide was used (Syndeco, Basel, Switzerland). Data were collected at the Canadian Light Source on beam line 08- ID1.

2.4.2 Data collection and processing

The crystals belong to the space group $P3_121$ and $P2_12_12_1$, with dimensions of $a = b = 110.81 \text{ \AA}$ and $c = 71.12 \text{ \AA}$. The asymmetric unit contains one tetramer ($V_M = 5.17 \text{ \AA}^3/\text{Da}$). The native data set was collected in-house at 100 K using an X-ray source ($\lambda = 1.5418 \text{ \AA}$) with RIGAKU rotating anode on a 30 cm RIGAKU R-AXIS IV plate detector. The RHCC mercury data set was collected at the Canadian Light Source (CLS) on beamline 08-ID1 at a wavelength of 0.8472 \AA on a 18 cm marCCD detector (Mar Research, Canada). Diffraction images were processed using the program suite MOSFLM (Leslie, 1994) and the CCP4

package (CCP4, 1994). Positional refinement was performed with CNS using the maximum likelihood method (Brunger et al., 1998). Refinement with CNS was alternated with manual electron density refitting of side-chains and terminal regions using MAIN (Turk, 1992). The target parameters of Engh and Huber, overall anisotropic B-factor scaling and bulk solvent corrections were utilized without applying non-crystallographical symmetry restraints. Water molecules added were chosen by distance criteria and hydrogen bonding geometry and were tested for position in spherical density, reasonable temperature factors, real space R-values, and improvement of the R-factors.

2.5 Circular Dichroism:

Far-UV circular dichroism spectra and melting temperature experiments were recorded using a Jasco-810 spectropolarimeter with a 0.1 cm pathlength quartz cuvette. All experiments were performed at a protein concentration of 0.2 mg/ml. The buffers used varied depending on the pH of the aqueous medium. However the ionic strength was kept constant at 154 mM except for the measurement series made with ultra pure water.

2.5.1 CD Instrument calibration

Calibration of the CD instrument was performed as described in Meier (2009). This procedure uses 2.583 mM (IS)-(+)-camphor-10-sulfonic acid (CSA) for the calibration of the magnitude of the CD signal, with the CSA peaks measured at 290.5 nm and 192.5 nm in a 1 mm quartz cuvette at 20°C. A baseline correction was also performed using ultrapure water. The instrument's correction factor and performance were calculated using the CD signals at 192.5 nm and 290.5 nm as described by the equations below.

$$c = CD_{290.5 \text{ nm obs}} / CD_{290.5 \text{ nm ref}} \quad (\text{Eqn. 2.8})$$

$$\text{abs}(CD_{192.5 \text{ nm}} / CD_{290.5 \text{ nm ref}}) > 2.05 \quad (\text{Eqn. 2.9})$$

where c is the correction factor, $CD_{290.5 \text{ nm obs}}$ and $CD_{290.5 \text{ nm ref}}$ are the observed and literature reference value of the CD signal at 290.5 nm. The parameters for spectrum and variable temperature measurements were followed as described (Meier, 2009).

2.5.2 RHCC sample measurements and data processing

CD data was collected on the Jasco-810 spectropolarimeter (Jasco, U.S.A.). The protein was dissolved in phosphate buffered saline (10 mM phosphate, pH 7.5 and pH 2, 154 mM sodium chloride) or Capso buffer (10 mM Capso, pH 10.0, 154 mM sodium chloride).

The mean residual ellipticity ($[\theta]_{\text{mrw}}$) was calculated with the formula below;

$$[\theta]_{\text{mrw}} = \theta / (c.l.n) \quad \text{Eqn (2.10)}$$

where θ is the measured ellipticity in millidegrees, c is the molar protein concentration in molar, l is the optical path length of the cuvette in millimeters and n is the number of peptide bonds.

The alpha helical content was determined by measuring the ellipticity at 222 nm using the formula below (Taylor *et al.*, 1987).

$$\alpha = (\theta_{222} - \theta_{r, 222}) / (\theta_{\alpha, 222} - \theta_{r, 222}) \quad \text{Eqn (2.11)}$$

where α is the helical fraction, θ_{222} is the measured ellipticity at 222 nm. A value of $\theta_{\alpha, 222} = -36,000$ would correspond to an ellipticity of a fully helical protein, whereas $\theta_{r, 222} = 3000$ is the ellipticity for an unstructured protein.

Melting experiment data were fitted to the cooperative thermodynamic two state

monomer dimer model as described Greenfield using the Levenberg – Marquardt optimization (Marquardt *et al.*, 1963; Greenfield *et al.*, 2004). In summary the data were fitted to the equation;

$$\theta_{222,T} = \alpha_T(\epsilon_F - \epsilon_U) + \epsilon_U, \quad (\text{Eqn 2.12})$$

where $\theta_{222,T}$ is the measured CD at temperature T, α_T is the α -helical fraction at temperature T, ϵ_F and ϵ_U are the CD of the folded and unfolded protein respectively.

2.5.3 Spectrum measurements

All spectrum measurements were performed between 180 nm – 250 nm in triplicate at 20°C except otherwise stated. The triplicate spectra were averaged and subtracted to give the Far-UV absorption reading for RHCC molecule (Far-UV Abs_{RHCC}). The formula is described below:

$$\text{Far-UV Abs}_{\text{RHCC}} = \text{RHCC}(\text{Abs}_{180\text{nm}-250\text{nm}}) - \text{Buffer}(\text{Abs}_{180\text{nm}-250\text{nm}}) \quad (\text{Eqn. 2.13})$$

where $\text{RHCC}(\text{Abs}_{180\text{nm}-250\text{nm}})$ and $\text{Buffer}(\text{Abs}_{180\text{nm}-250\text{nm}})$ are the Far-UV absorbance readings for RHCC in buffer and buffer alone, respectively.

2.5.4 Variable temperature measurements

CD melt measurements on the Jasco-810 instrument were performed by varying the internal temperature of the cuvette containing RHCC sample using a peltier device. In addition to the peltier, was an external water bath which served as a backup temperature control system. An RHCC concentration of 0.2 mg/ml was used for all measurements.

2.6 Bioremediation of Hg²⁺ ion from aqueous solution

2.6.1 Mercury stock preparation

10 mg of solid mercury nitrate and di-potassium mercuric iodide were accurately weighed using an analytical balance and dissolved into 50 ml ultra pure water. The final concentration of mercury in the stock solution was 200 mg/L. All the dilution series used in these experiments were prepared from these initial stock solutions as required.

2.6.2 Preparation of RHCC

For all the mercury binding experiments a RHCC concentration of 0.1 mg/ml was used. RHCC stock solutions were prepared as described earlier. The protein stock was filtered through a 0.2 µm filter and all mercury binding experiments were performed in a buffer containing 10 mM sodium phosphate, pH 7.5, 154 mM NaCl.

2.6.3 Biosorption of Hg²⁺ ions by RHCC using dialysis method

2.6.3.1 Dialysis method

This technique involves the use of a standard regenerated cellulose (RC) membrane with a 3,500 Da cut-off (Spectrum Laboratories Inc U.S.A). Prior to dialysis, the membranes were soaked in a cleaning buffer (1 % SDS, 1 % EDTA) for 15 min, to eliminate all traces of metal ions associated with the dialysis membrane. Then the dialysis membrane was thoroughly washed with ultra pure water to remove any trace of the cleaning buffer. A sample of RHCC was then placed into the dialysis membrane and dialyzed against 300 ml of buffer containing mercury (Fig. 2-2).

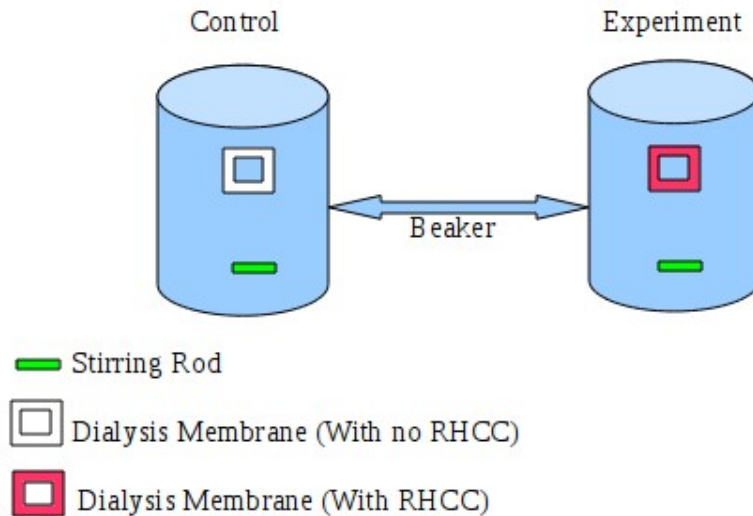


Figure 2-2: A simple dialysis setup, showing the control and experiment. Aqueous buffers [10 mM sodium phosphate, pH 7.5, 154 mM sodium chloride] were spiked with mercury compounds and incubated over 24 hrs interval.

2.6.4 Sample collection and storage

Mercury concentrations were diluted from mercury stocks using a filtered 10 mM sodium phosphate buffer pH 7.5, 154 mM NaCl to an equal volume (300 ml) for both control and experiment. A 0.1 mg/ml concentration of the RHCC was added to the experiment membrane and only buffer to the control membrane. Aliquots (15 ml) were collected after 24 hours to detect the mercury concentration using the Cold Vapour Atomic Fluorescence Spectrometry (CVAFS). Aliquots were spiked with the oxidizing reagent bromine monochloride (BrCl) in a ratio of 5:1 (v/v) to ensure that all mercury atoms are in their oxidized ionic (Hg^{2+}) form. Samples containing mercury were tightly sealed to prevent evaporation. All samples were stored at 4 °C, until they were ready to be analyzed. Replicates were performed for both controls and experiments with samples collected and preserved as described above

(Method 1631, Revision E: Mercury in Water by Oxidation, Purge and Trap, and Cold Vapour Atomic Fluorescence Spectrometry). The percent biosorption of the Hg^{2+} ions were calculated using Equation 2.8 (see below):

$$\text{Biosorption (\%)} = (C_i - C_f) / C_i \times 100 \quad (\text{Eqn. 2.14})$$

where C_i and C_f are the initial and final metal ion concentrations, respectively (Sari *et al.*, 2009).

2.6.5 Mercury detection using Cold Vapour Atomic Fluorescence Spectrometry (CVAFS)

2.6.5.1 Summary of method

All calibration, standardization and detection of mercury were performed by the Ultra Clean Trace Element Laboratory (UCTEL). Prior to analysis as earlier mentioned, all mercury is oxidized to Hg^{2+} with BrCl . Samples are diluted to the range of detection by the instrument. The samples are then reduced with $\text{NH}_2\text{OH}\cdot\text{HCl}$ to destroy any free halogens, present before reduction with stannous chloride (SnCl_2) to convert Hg^{2+} to volatile Hg^0 . The Hg^0 is separated from the solution either by purging with nitrogen, helium or argon gas or by vapour/liquid separation. Any Hg^0 present is collected onto a gold trap. The Hg is thermally desorbed from the gold trap into an inert gas stream that carries the released Hg^0 to a second gold (analytical) trap. The mercury is desorbed from the second trap into a gas stream that carries the Hg into the cell of a cold vapour atomic fluorescence spectrometer (CVAFS) for detection.

2.7 Statistical analysis

Data were analyzed by using the Gnumeric spreadsheet and the two-tailed Student's t-test was used for the comparison with a control. To determine the t-value the Equations below were used.

$$S_p = [((n_1-1)\sigma_1^2 + (n_2-1)\sigma_2^2) / (n_1+n_2-2)]^{1/2} \quad (\text{Eqn. 2.15})$$

$$T_{\text{value}} = [(\bar{x}_1 - \bar{x}_2) / (S_p \times (n_1^{-1} + n_2^{-1}))] \quad (\text{Eqn. 2.16})$$

where S_p is the pooled standard deviation, n_1 and n_2 are the number of separate replicate performed for experiment and control, respectively. Also σ_1^2 and σ_2^2 are the variances for experiment and control, respectively. And \bar{x}_1 and \bar{x}_2 are the mean of the replicated for experiment and control, respectively.

All P values were determined from the t distribution table, taking into consideration the degree of freedom. $P_{\text{value}} < 0.01$ were considered statistically significant which means that there is a significant difference between two population.

3. RESULTS AND DISCUSSION

3.1 Purification of the RHCC protein in the cytoplasm of *E. coli*

From a 1.6 L bacterial culture, 40 mg of pure RHCC was obtained. The pure protein was analyzed by Tricine SDS-PAGE (Fig. 3-1) which revealed the presence of a series of bands corresponding to RHCC (Fig. 3-1).

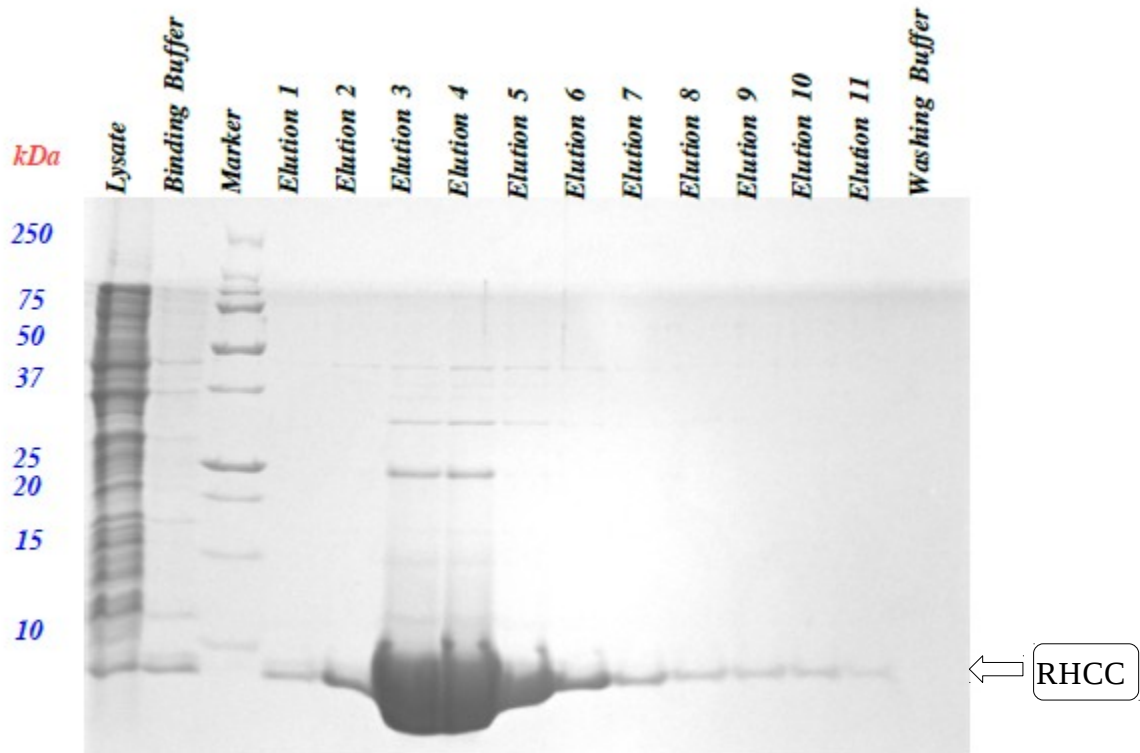


Figure 3-1: Purification of RHCC by Ni-NTA affinity column. Proteins samples were run on a 16 % Tricine SDS-PAGE gel and stained with Coomassie Blue. The lysate and the fractions eluted from the Ni-NTA column are indicated along the top of the gel.

The purification of RHCC could be performed at room temperature without any detectable degradation (Fig. 3-1). Histidine tagged RHCC runs as a 7.8 kDa band on the gel. To each protein fraction, a total of 5 mM EDTA was added to chelate any traces of nickel that might have leached from the column.

3.1.2 Proteolysis of Histidine tag

In order to remove the Histidine tag, the protease thrombin was used. A time course experiment showed that full cleavage of the His₆-tag required an incubation time of 16 hours at room temperature. Furthermore, 1 unit of thrombin is sufficient to cleave 1 mg of RHCC under these conditions (Fig. 3-2).

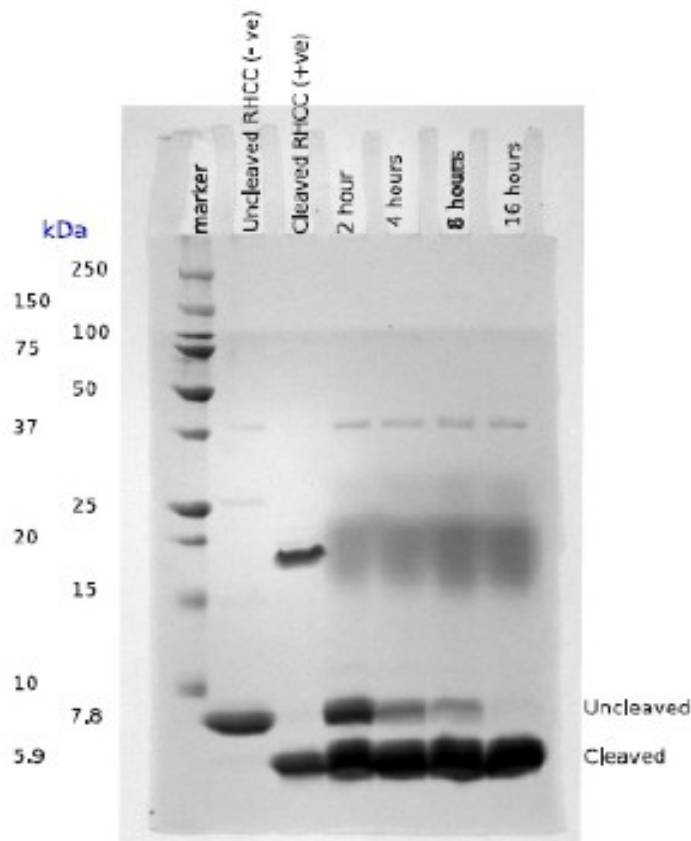


Figure 3-2: Proteolytic cleavage of His₆-tag from RHCC. Aliquots of the cleaved protein at different incubation times (2, 4, 8 and 16 hrs) were run on a 16 % Tricine SDS-PAGE gel. Complete proteolysis is obtained after 16 hrs. The lanes containing M_w marker, negative control (uncleaved RHCC) and positive control (cleaved RHCC) are indicated along the top of the gel.

3.1.3 Western blotting

We verified that the His₆-tag had been fully removed by performing a Western Blot analysis of the digested protein. Probing samples of the RHCC digested with thrombin for 2, 4, 8 and 16 hours with a penta-His antibody confirmed the result presented on the previous page, namely that it is necessary to incubate the protein with thrombin for 16 hours to fully remove the His-tag (Fig. 3-3).

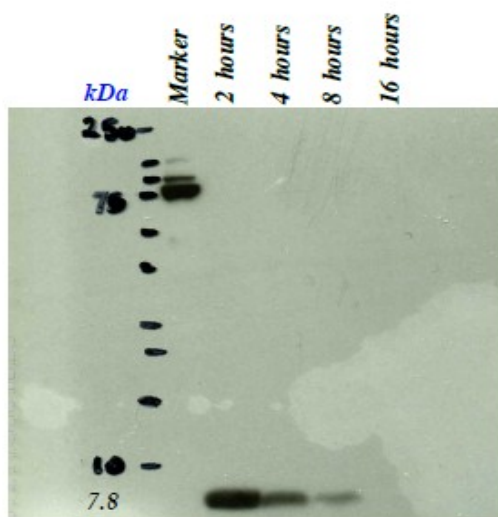


Figure 3-3: Analysis of Thrombin digested RHCC by Western Blotting. The presence of His-tagged RHCC was detected by a Penta-His antibody conjugated to HRP and developed using the ECL kit (GE Healthcare). An exposure time of 150 seconds was used.

3.1.4 Determination of the size and homogeneity of RHCC by DLS

The R_H of RHCC was measured by DLS to be 2.70 ± 0.10 nm which is slightly larger than the theoretical R_H (R_H^{Theo}) of 2.18 nm calculated from Eqn 2.7. This is not entirely unexpected given that RHCC is an α -helical protein. Helical proteins of a given molecular

weight will always give a larger than expected R_H value due to their extended structure. However, the DLS analysis was useful in that it showed the purified protein to be homogeneous (Fig. 3-4) and thus suitable for crystallization.

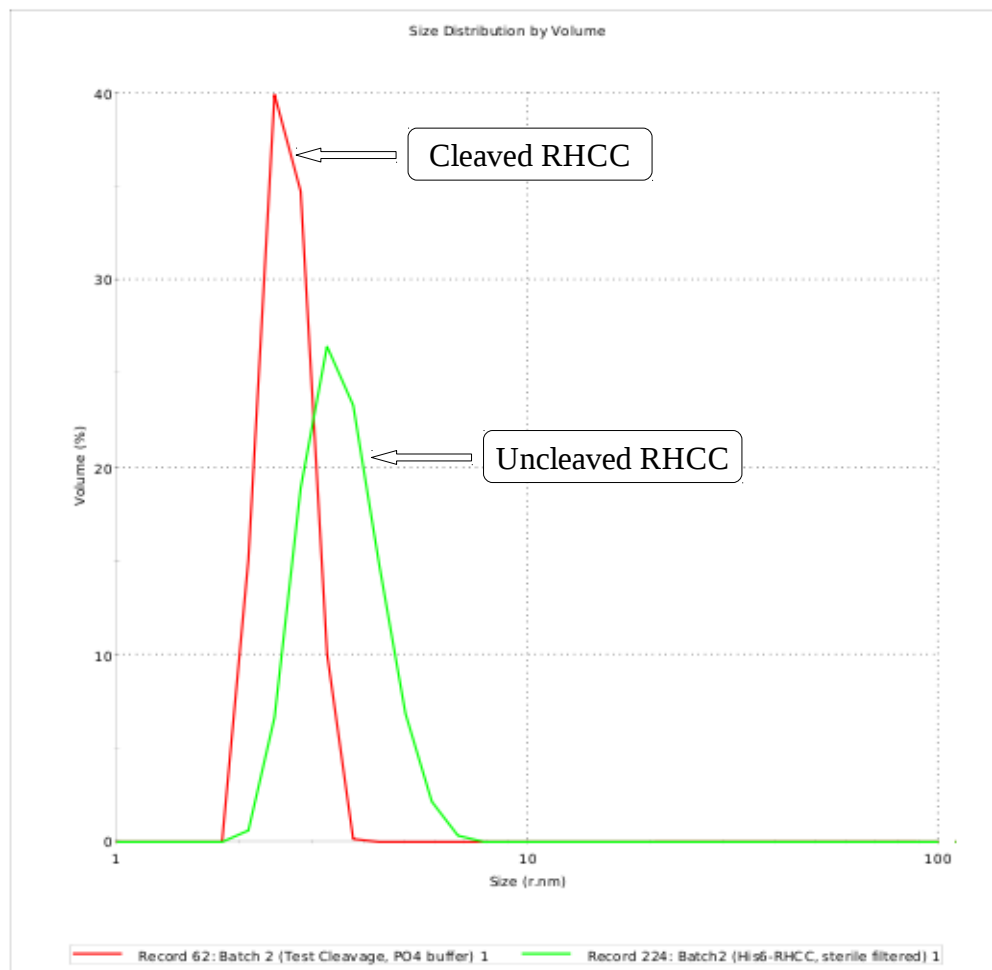


Figure 3-4: Size measurement of RHCC by DLS instrument. The percent volume of cleaved and uncleaved RHCC are represented in red and green, respectively. The hydrodynamic radius is on x – axis and percent volume on y – axis.

In agreement with the SDS-PAGE data (Fig. 3-2) the result from DLS also show that the cleaved RHCC is smaller than the His₆-tagged RHCC (Fig. 3-4). In addition, the

hydrodynamic radius of RHCC calculated by DLS remained constant at 2.7 ± 0.05 nm for protein concentrations in the range 1-9 mg/ml (Fig. 3-5). Therefore, we can clearly state that the RHCC protein does not undergo concentration dependent aggregation.

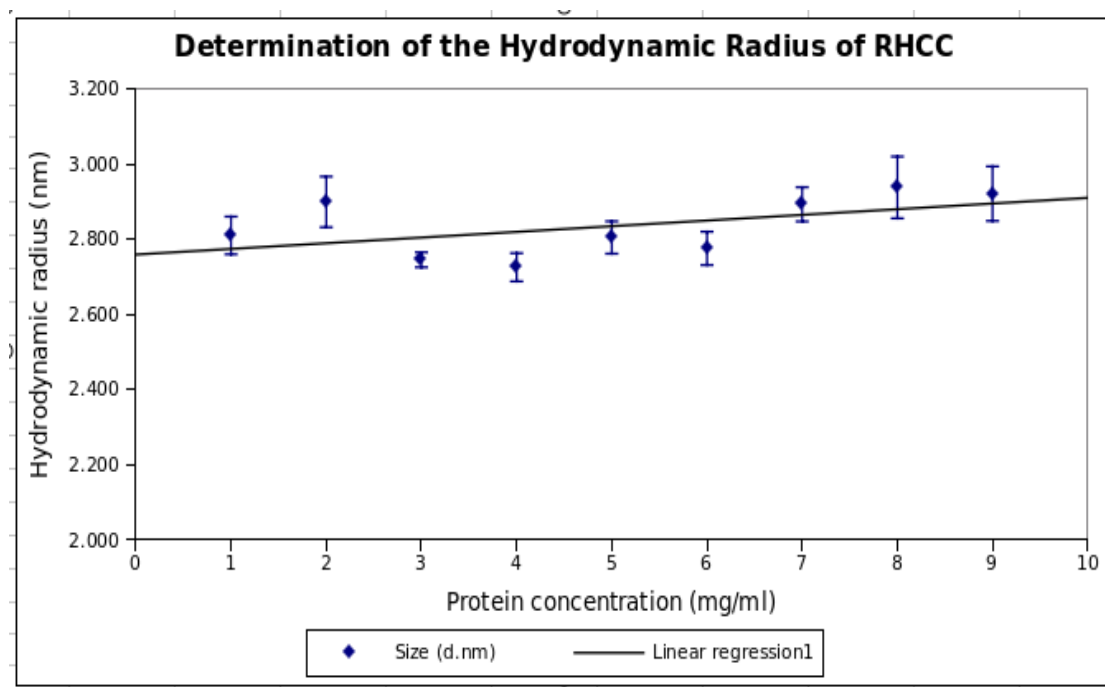


Figure 3-5: Hydrodynamic radii of RHCC obtained at 20 °C in ultrapure water as a function of the protein concentration.

3.2 X-ray Crystallography of native RHCC

A prerequisite for high resolution X-ray data are crystals of excellent quality with the right spacegroup for inhibitor scans. However, it is often difficult to obtain, in refinement protocols of crystallization conditions, the right composition like precipitating agents, drop sizes, temperatures and additives. We performed here a systematic screen for new crystallization conditions with the aim to obtain different spacegroups with the purpose of varying crystal lattice forces. In addition, we wanted to alternate the content of the four large cavities in the right-handed coiled coil to see if crystallization affects the content of the cavity. Right handed coiled-coil tetramer has been re-crystallized by the vapour diffusion method as previously mentioned. Crystallization conditions were performed with 200 mM ammonium acetate as crystallization agent and 100 mM Tris-HCl (pH = 8.5), but at different concentrations of isopropanol (Fig.3-6). The crystals diffracted between 2.0-2.4 Å at room temperature. The obtained crystal form was orthorhombic, and had unit-cell edges of $a = 34 \text{ \AA}$ $b = 65 \text{ \AA}$ $c = 110 \text{ \AA}$ with a space group $P2_12_12_1$.

Furthermore, we studied the space group changes, crystal lattices and crystal contacts to derive a possible mechanism for large-scale screens of potential cargo systems. Many applications based on structural information like trapping of catalytic intermediates in enzyme catalysis or analysis of protein-protein interaction mechanisms request high resolution information (for a comment see Harrison, 2004). Thereby, the bottleneck for X-ray crystallographers is not anymore the *de novo* determination of a protein structure but a methodological approach to high-resolution information of excellent quality in a crystal lattice environment allowing cocrystallization attempts. We proposed that the replacement of ammonium sulfate by any other counter ion (e.g. acetate or phosphate) to an already established protein crystallization setup might mediate favourable crystal contacts with the

consequence of getting better diffracting crystals, alternated crystal lattice contact points and different contents of the four large cavities.

(A)



(B)



Figure 3-6: RHCC protein crystals. Crystals grew at 20 °C for one week. (A) RHCC crystal at a condition containing 26 % isopropanol. (B) Crystals obtained under similar condition with 30 % isopropanol.

3.2.1 Crystals and X-ray diffraction

Initial setups of growing RHCC crystals in the presence of ammonium acetate showed that the crystallization behaviour was significantly different to the previous conditions. The fact that the crystal size, morphology and spacegroup changed suggested for a new symmetry with different crystal contacts. Test series of different dilutions for the additive were not indicative for a certain concentration limitation. The diffraction limit on the in-house X-ray source was about 2.0 Å and a complete data collection statistics are given in Table 3-1.

Table 3-1: Data collection and refinement statistics between RHCC at 1.4 Å (spacegroup P3₁21) and 2.0 Å (spacegroup P2₁2₁2₁) resolution-both measured using the in-house rotating anode. All data sets were measured at 100K.

Data collection statistics¹		
X-Ray source	in-house	in-house
	(1.5418Å)	(1.5418Å)
Resolution (Å)	1.4 (1.49-1.40)	2.0 (2.18-2.0)
Observed reflections	804598	79623
Unique Reflections	86287	11500
Completeness	96.6 (96.6)	97.3 (96.4)
R _{sym} ²	6.3 (37.0)	7.4 (31.0)
Wilson B-factor (Å ²)	22.19	27.5
<I/σI>	14.6 (2.7)	20.3 (8.7)
Refinement statistics		
R _{factor} ³ (%), no sigma cutoff	21.1 (28.9)	19.9 (24.1)
R _{free} (%), no sigma cutoff	22.6 (29.9)	23.5 (28.3)
Mean B factor (Å ²)		
Protein atoms	18.8	17.86
Water molecules	41.3	38.9
Bonds (Å) ⁴	0.004	0.004
Angle (°) ⁴	0.7	0.72
Ramachandran Plot ⁵	100/ 0/ 0/ 0	100/ 0/ 0/ 0

¹Final shell in parenthesis. ²R_{sym} = $\sum |I - \langle I \rangle| / \sum I$. ³R_{factor} = $\sum ||F_{obs}| - |F_{calc}|| / \sum |F_{obs}|$. ⁴Root-mean-square error.

⁵Percentage of residues in most favoured/ additional allowed/ generously allowed and disallowed regions of the Ramachandran plot.

3.2.2 Crystal lattice contacts

The structure of RHCC in the space group $P2_12_12_1$ was solved using the native RHCC structure (Protein Data Bank code 1FE6) as a search template (Fig. 3-7). Table 3-1 summarizes the crystallographic refinement statistics. The low overall B-factor for the protein atoms only (18.8\AA^2) indicates a rigid protein structure. Remarkably, only Asp21 and Ser25 in subunits A, B and D show alternative conformations which suggests that there is more flexibility within this region of the protein. A $C\alpha$ -atom superposition with the previously determined RHCC structure (pdb-code:1FE6) shows that in current work, the structure determined is identical to the original RHCC structure (rmsd of 202 $C\alpha$ atoms: $< 0.2\text{\AA}$). The RHCC chain fragment forms a parallel right-handed coiled-coil tetramer with an average length and diameter of 72\AA and 25\AA , respectively. RHCC has been shown to form a regular meshwork-like arrangement in the hexagonal setting of the crystal lattice. RHCC crystals have only 25 % protein content and are consequently very loosely packed.

In the previous $P3_12_1$ spacegroup the crystal contact face between symmetry related molecules is very close with 6 symmetry equivalent molecules in the asymmetric unit. All helical segments are involved in numerous crystal contacts blocking access to the storage cavities. In the new $P2_12_12_1$ spacegroup less than 5% of the solvent accessible surface area is involved in crystal contacts. As shown in Figure 3-7B, only four symmetry equivalent molecules are in the asymmetric unit, which results in a much looser overall crystal packing. Surprisingly given these changes in crystal packing the new RHCC crystal form diffracts almost as strongly as the original crystal form. An interesting observation is that access to the storage cavities is much more open in the new crystal form and so we might consider investigating the potential of RHCC to bind other potential cargos, as we will see later.

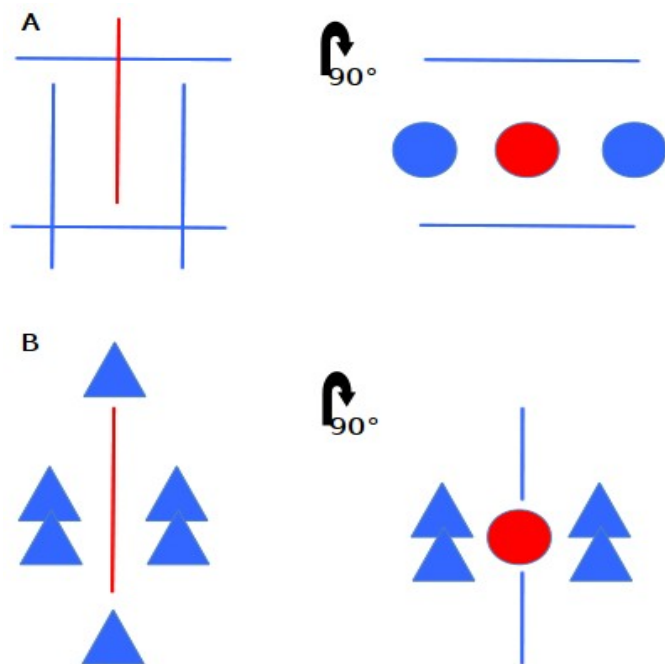


Figure 3-7: Comparison of crystal contacts between RHCC in spacegroup P212121 (A) with RHCC in spacegroup P3121 (B). Two orientations are compared. The left side shows the tetrameric channel in along the central helical axis, with the N-terminus at the bottom. The right side shows a perpendicular orientation from N- to C-terminus. The RHCC molecule in the asymmetric unit is in red; crystal symmetry neighbours are drawn in blue.

3.2.3 Cavity content

The addition of acetate instead of sulfate into the crystallization mix with the aim to optimize crystal contacts between symmetry equivalent molecules revealed also consequences on the content of the storage cavities (Fig. 3-8). Four large cavities ranging in volume between 145 Å³ and 300 Å³ are placed in regular distances along the strictly hydrophobic channel of the RHCC tetramer. Two types of “knobs-into-holes” interactions at positions **a** and **h** corresponding to a 7,4-motif of core residues. In addition, the RHCC structure shows in positions **e** and **k** predominantly hydrophobic amino acids (Fig. 3-8). They together form a very extensive hydrophobic interhelical interface. Of the large number of charged residues within the RHCC sequence (about one third of all amino acids), with two exceptions (Asp6 and Glu43) all are involved in salt bridge formation, either intrahelically or interhelically (Stetefeld et al., 2000). The salt bridges are organized in three complex networks forming layers that surround the tetrameric cylinder at the height of the cavities (Fig. 3-8). Instead of fully occupied clathrate like cluster the cavities are more or less empty. It remains unclear though if this is a consequence of different diffusion properties of the counter ion or a hint for incorporation of sulfate inside the cavities. Further experiments are required in this direction.

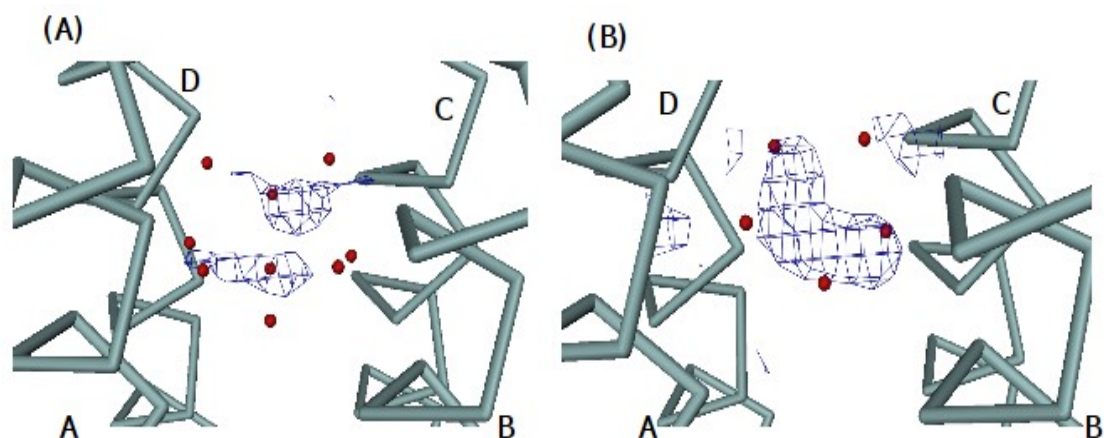


Figure 3-8: Superposition of the final refined 2DFo-mFc map at 2 Å resolution (1.5 σ contour level) onto the crystal structure containing water cluster (Stetefeld 2001, pdb-code 1FE6). Four helical segments (A-D) are shown as grey C α -traces in render mode. Individual water cluster are shown as red coloured spheres.

In conclusion, the aim of this study was to explore the ability of changing the crystallographic spacegroup by altering the crystallization agent as potential mediator of favourable crystal contacts. Our data suggest the use of ammonium acetate and Isopropanol as additive to improve the crystal quality without changing already established crystallization conditions. To expand our experience, projects using CAPB for more tightly packed crystals and as an additive in primary screening protocols are still in progress.

3.3 RHCC thermo-stability based on pH and thermal denaturation

In this section, the focus was to determine why RHCC is so thermostable. It is already well known that coiled coils are largely stabilized by the distinctive packing (knobs-into-holes) of hydrophobic residues positioned at the 'a' & 'd' and 'a' & 'h' positions in left and right handed coiled-coils, respectively. However, there are also a number of key ionic interactions that are observed between the helices in a coiled coil that are also likely to be important for the thermal stability of coiled coils. It seems probable that the increase in stability can be linked to an increase in the number of hydrogen bonds (Scandurra, *et al.*, 1998). Therefore, in this section we will focus on the role ionic interactions plays in the additional thermostability observed in coiled coils.

Ion pairs were first proposed by Perutz in the mid 70s as being important for protein stabilization (Perutz *et al.*, 1975; 1978). Perutz explained that most thermophilic bacteria owe their extra stability to the formation of external salt bridges on the protein surfaces (Perutz *et al.*, 1978). There have been other reports to show the positive effects of salt bridges increase in the stability of hyperthermophilic proteins (Delboni *et al.*, 1995). However, it is important to point out that not all ion pairing will enhance the stability of a protein, as some might actually destabilize the protein (Hendsch, *et al.*, 1994; Honig, *et al.*, 1995). The presence of ion pair between charged residues in the interior core of proteins can destabilize their tertiary structure whereas similar pairing on the external surface of the protein increases the stability.

Relevant to this work, are two different classes of ionic interaction that enhance the thermostability of their tertiary structures. The first class stabilizes the individual α -helix and act therefore intra-helically. The other class of ionic interaction leads to the formation of the coiled-coil oligomer and thus act interhelically. These are described as follows;

3.3.1 RHCC intrahelical and interhelical ionic interaction

The formation of ionic interactions within the α -helices of RHCC is the first step to forming the coiled-coil oligomer. The intrahelical interaction help stabilize the monomeric α -helix. The sequence of RHCC consists of a high content of charged residues, approximately one-third of the overall sequence (Chapter 1, Fig 1-3). Based on the distance between charged residues all except the Glu6 and Asp43 are able to form intrahelical and/or interhelical salt bridges (Stetefeld *et al.*, 2000). There are seven (3 intrahelical , 4 interhelical) salt bridges per α -helix and all are occupied in the overall RHCC tetramer. Uniquely, this high frequency of electrostatic interaction has not been observed in any other coiled-coil structure and this may be explained based on the hyperthermophilic nature of the protein (Stetefeld *et al.*, 2000), an attribute that differentiates them from mesophilic coiled-coil proteins (Perutz *et al.*, 1978).

Stetefeld *et al.*, 2000 reported that the RHCC tetramer has the classical $i, i + 3$ (Glu24 – Lys27; $f - i$) and $i, i + 4$ (Asp10- Arg14; $g - g$ intrahelical salt bridges plus an additional $i, i + 1$ favourable electrostatic interaction between Asp21 and Arg22 ($c-d$) that is observed in the RHCC tetramer (prime indicates residue for an adjacent chain) (Fig. 1). Besides these two $i, i' + 2$ type interhelical ion pairs (Arg33 – Asp35', $d - f'$; and Asp36 and Glu38', $g - i'$) have been noticed in the crystal structures of p-LI mutant of the GCN4 leucine zipper and COMPcc (Harbury *et al.*, 1993; Malashkevich *et al.*, 1996), the RHCC tetramer demonstrate two types of interhelical electrostatic interaction not present in any coiled coil structure. Different from the usual inter-chain salt bridges that span one and two hydrophobic core layers, there is no core layer positioned between Asp20 and Arg22' ($i, i' + 2; b - d'$) (Fig. 3-9) and only one positioned between Asp9 and Arg14' ($i, i' + 5; f - g'$) (Stetefeld *et al.*, 2000).

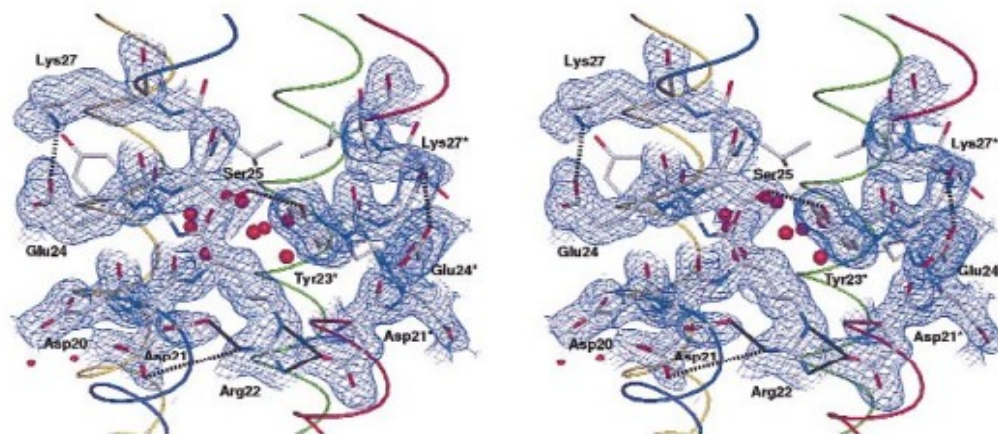


Figure 3-9: The 1.8 Å resolution electron density map of a fragment of the RHCC tetramer. Stereo view of a portion showing intrahelical (Lys27 – Glu24) and interhelical (Asp21 – Arg22) salt bridges. Dotted lines are the ionic interactions. Helices are in colour as Fig 1-3. The nine water clusters are represented as red spheres (Stetefeld *et al.*, 2000, please see attached appendix for copyright permission).

The overall thermostability of the RHCC was investigated by monitoring changes in the far UV spectral region (190-250 nm) by CD. By measuring the differential absorption signals in the pH range 2-10 and at 20 °C and 90 °C we could monitor any change in secondary structure under these conditions. In addition, we also calculated the melt point (T_m) under the various conditions used. Data were analyzed by comparing the difference in ellipticity at 222 nm, which relates to the helical content, taking into account the chain length dependence for CD signal of helix protein.

3.3.2 Far-UV spectrum and thermal denaturation profile

3.3.2.1 RHCC in water pH 7.0

When the RHCC sample was in pure water at 20 °C the CD spectrum (Fig. 3-10) showed two clear α -helical peaks at 222 nm and 208 nm which are characteristic of an α -

helical protein. Upon heating to 90 °C the α -helical content drops by approximately 30 % with the minima at 222 nm and 208 nm clearly visible. When the protein was subsequently cooled back to 20 °C the CD spectrum returned to within 10 % of the original signal indicating that under these conditions the protein was able to reversibly fold and unfold.

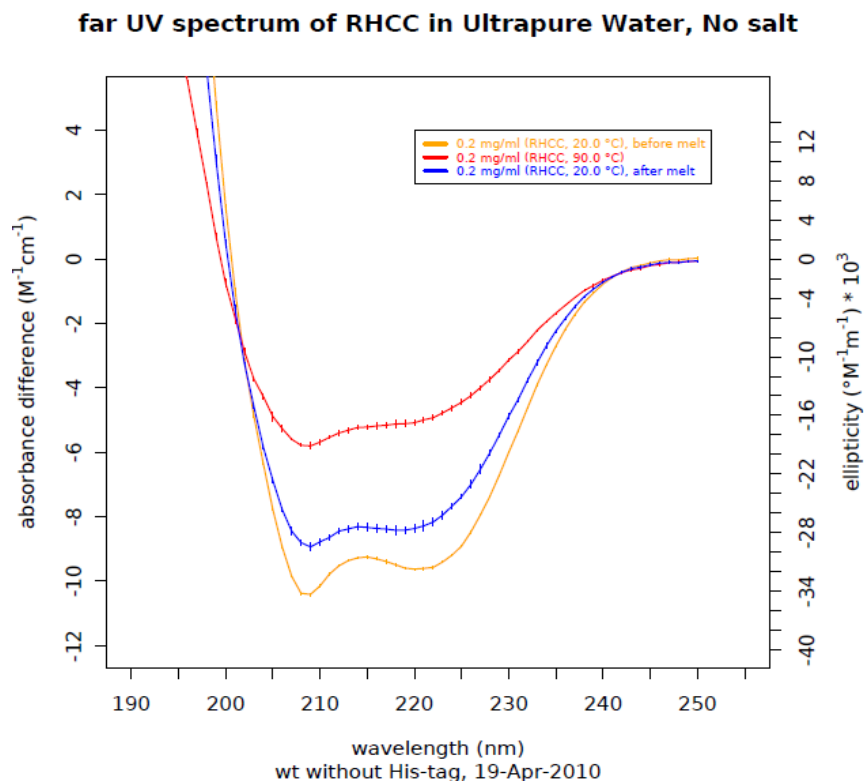


Figure 3-10: Far-UV CD spectra of RHCC in water. The spectra were recorded at a peptide concentration of 0.2 mg/ml. The differential absorbance and ellipticity of RHCC in pure water at 20 °C before melt (blue), 90 °C at melt (red) and 20 °C after melt (orange) are also shown.

Finally, at the 222 nm wavelength, a decrease in the molar ellipticity (ϵ) was observed at increased temperature (90 °C). Prior to melting the value for ϵ was $-31557 \text{ M}^{-1}\text{m}^{-1}$ whereas at 90 °C it had decreased to $-16239 \text{ M}^{-1}\text{m}^{-1}$. After re-cooling to 20 °C the value for ϵ was -26915

$M^{-1}m^{-1}$ which was slightly lower than its initial value. This result indicates that the protein partially unfolds upon heating to 90 °C but is able to refold to its starting state upon cooling back to 20 °C (Fig. 3-10). Thus under these conditions thermal stress was insufficient to cause an irreversible unfolding of RHCC.

3.3.2.2 RHCC in aqueous buffer pH 10.0

Analysis of the thermostability from the far-UV spectra generated for RHCC at pH 10.0, suggest an increase in the stability of the RHCC (Fig 3-11). At pH 10.0, RHCC is negatively charged, with a net charge of -7. From analyzing the RHCC crystal structure it is clear that all the ionic salt bridges are still formed. This is possible, because even at this high value, the pH is still less than the pKa values for Arginine (pK = 12.5) and Lysine (pK = 10.5) residues, and so they can still form an ionic interaction with the Glutamic and Aspartic acid residues in the protein.

Based on our results (Fig 3-11) the value for ϵ at the 222 nm prior to melting (20 °C) was $-30407 M^{-1}m^{-1}$ and upon heating to 89 °C it decreased to $-22181 M^{-1}m^{-1}$. After melt the molar ellipticity became $-33761 M^{-1}m^{-1}$ at 20 °C, which was more than the initial reading prior to melting. This is unusual and can happen if we lose some of the aqueous buffer by evaporation, which causes an increase in protein concentration. An increase protein concentration results in a higher absorbance difference of the polarized light.

far UV spectrum of RHCC in 10 mM Capso, I=154mM, pH 10.0

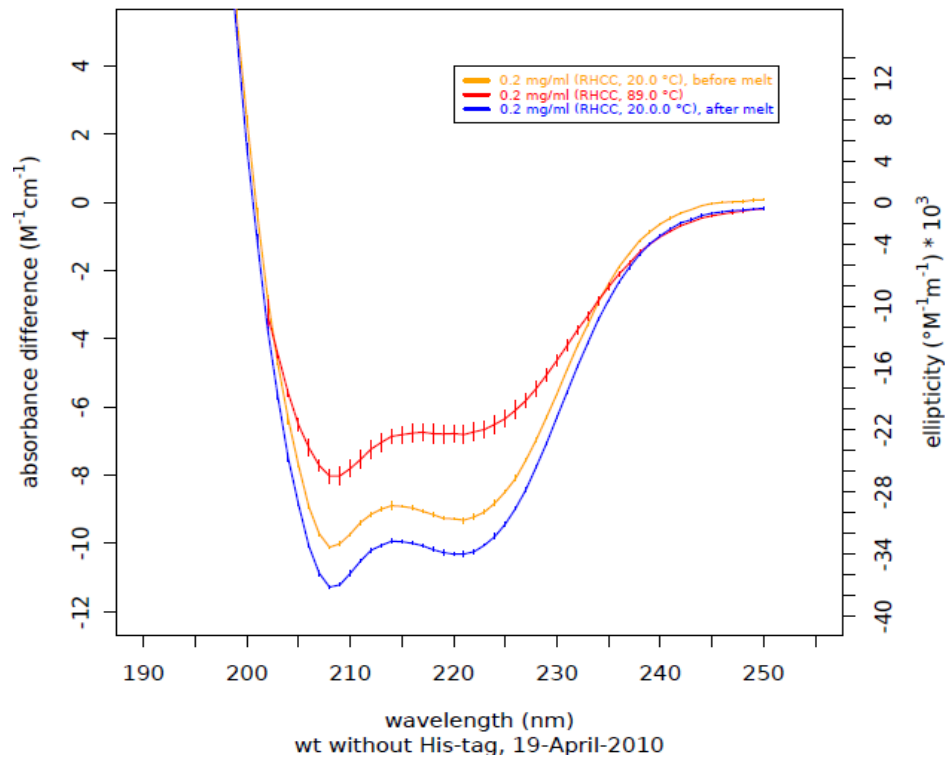


Figure 3-11: Far-CD spectra of RHCC at pH 10.0. The spectra were recorded at a protein concentration of 0.2 mg/ml. Far-UV spectra showing the differential absorbance and ellipticity of RHCC in a pH 10.0 aqueous buffer. Measurements were at 20 °C before melt (blue), 89 °C at melt for pH 10.0 analysis respectively (red) and 20 °C after melt (orange) are also shown.

3.3.2.3 RHCC in aqueous buffer at pH 2.0

far UV spectrum of RHCC in 10 mM sodium phosphate, pH 2.0

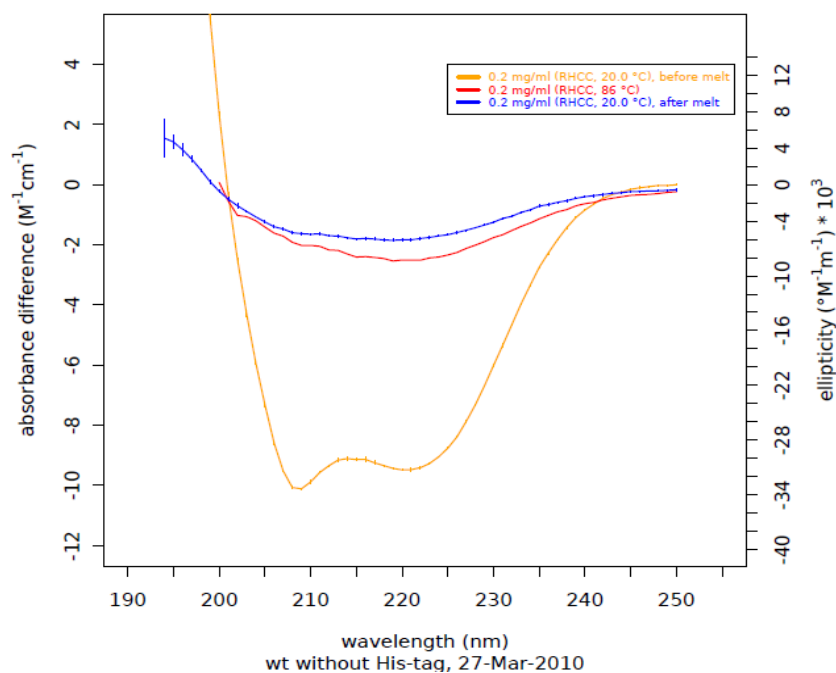


Figure 3-12: Far-CD spectra of RHCC at pH 2.0. The spectra were recorded at a protein concentration of 0.2 mg/ml. Far-UV spectra showing the differential absorbance and ellipticity of RHCC in a pH 2.0 aqueous buffer. Measurements were at 20 °C before melt (blue), 86 °C at melt for pH 2.0 analysis respectively (red) and 20 °C after melt (orange) are also shown.

Analysis of the far-UV spectra of RHCC in an acidic environment at pH 2.0 showed that RHCC was irreversibly denatured at 86 °C (Fig 3-12). At this pH, RHCC has a net charge of +6, due to the protonation of the previously unprotonated Glutamic acid and Aspartic acid residues. This means that the salt bridges between the Glu/Asp and Arg/Lys residues are unable to form. As a result of the loss of these interactions the thermostability of the protein was significantly reduced. A similar case reported for the SH3 domain of ESP8 (Kishan *et al.*,

2000), where disruption of a key intermolecular salt bridge between Glu22 and Arg18 prevented the SH3 domain from forming a dimer.

We observed the molar ellipticity (ϵ) at 222 nm (Fig. 3-12) and our results show that the value for ϵ at 20 °C prior to melting was $-30104 \text{ M}^{-1}\text{m}^{-1}$ and upon heating to 86 °C it decreased to $-9828 \text{ M}^{-1}\text{m}^{-1}$. After re-cooling the molar ellipticity became $-5734 \text{ M}^{-1}\text{m}^{-1}$ at 20 °C, which was lower than the initial reading prior to melting. This means that the RHCC was denatured at melt and was unable to refold to its initial tertiary structure.

3.3.3 Thermal denaturation profile

Analysis of the denaturation profile (Fig 3-13) of RHCC at different pH clearly shows a thermolabile and thermostable state exists under acidic and basic conditions, respectively. These melting experiments show that RHCC falls into the class of thermophilic proteins known as thermoalkaliphiles (Wiegel *et al.*, 1998). Such organisms are capable of operating at pH values > 9.5 . At pH 10.0, our results show that at a high temperature of 86 °C the molar ellipticity is $-25,709 \text{ M}^{-1}\text{m}^{-1}$ compare to a value of $-9,828 \text{ M}^{-1}\text{m}^{-1}$ at pH 2.0. This tells us that the α -helical structure is better retained under alkaline conditions than under acidic conditions. From this data we can clearly state that the order of thermal denaturation for RHCC is pH 10.0 $>$ pH 7.0 $>$ pH 2.0. In support of this statement, a summary of protein conditions, molar ellipticity and percent change in ellipticity throughout the temperature series is shown in Table 3-2.

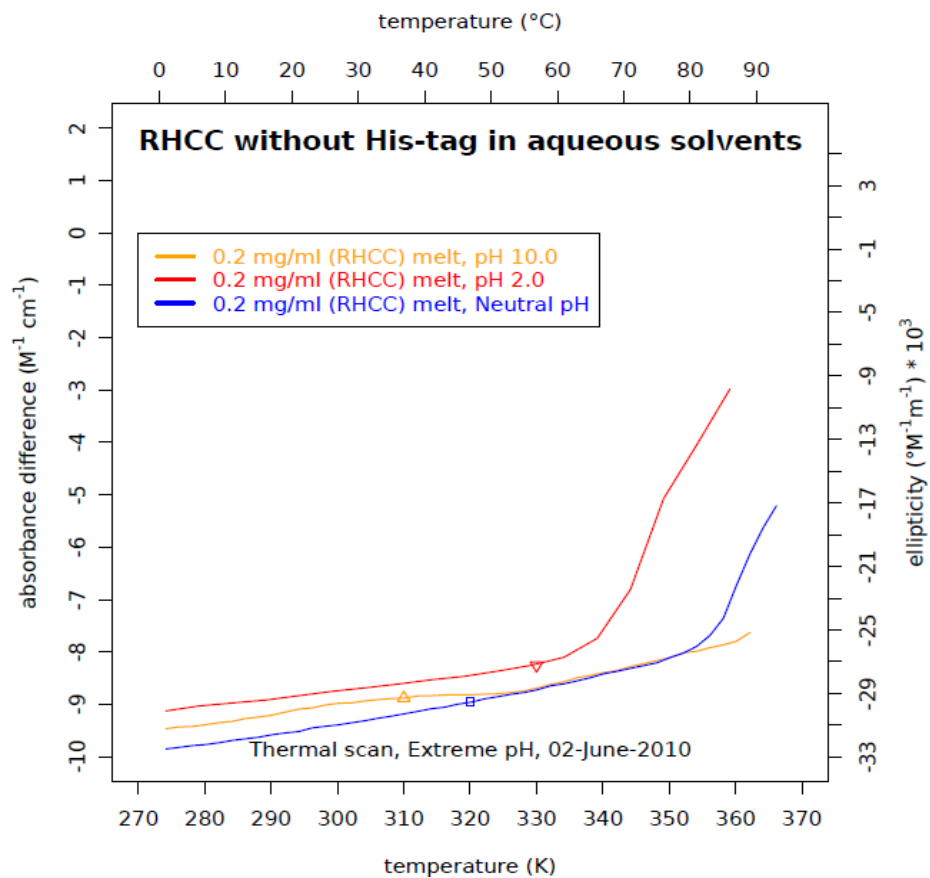


Figure 3-13: Thermal denaturation curves of RHCC measured at 222 nm. Temperature in Kelvin (x-axis1), Temperature in °C (x-axis2), absorbance difference in $M^{-1}m^{-1}$ (y-axis1), ellipticity in $M^{-1}m^{-1}$ (y-axis2). A temperature range of 1 °C to 90 °C was used, with the traces at pH 2.0 (red), pH 7.0 (blue), pH 10.0 (orange) shown.

Table 3-2: Summary of molar ellipticity and percentage change in ellipticity thermal scan signals of RHCC at 222 nm.

Aqueous Buffer Condition	Molar Ellipticity ($M^{-1}m^{-1}$)	%Δ ellipticity
Acidic (pH 2.0)	-30,104 at 1 °C	67.4
	-9,828 at 86 °C	
Neutral (pH 7.0)	-32,501 at 1 °C	31.7
	-22,182 at 86 °C	
Alkaline (pH 10.0)	-31,228 at 1 °C	17.7
	-25,709 at 86 °C	

Based on our results we show that, RHCC loses some of its ability to detect the difference in left and right polarized light due to the loss of chirality from the peptide backbone as the pH shifts from basic to acidic. The loss of chirality is due to the denaturation and unfolding of the RHCC α -helices as illustrated in the thermal denaturation profile (Fig.3-14). The profile indicates that the α -helical content of the RHCC is better retained at high temperatures under alkaline conditions than under acidic conditions. Due to the temperature limitation of the CD instruments we used, we could obtain the melting temperature (T_m) for RHCC at pH 2.0. At this pH RHCC has a T_m of 82 °C which places it into the extreme class of thermostable proteins. Whilst we could not determine the actual T_m for RHCC at either pH 7 or pH 10, it is definitely in excess of 100 °C.

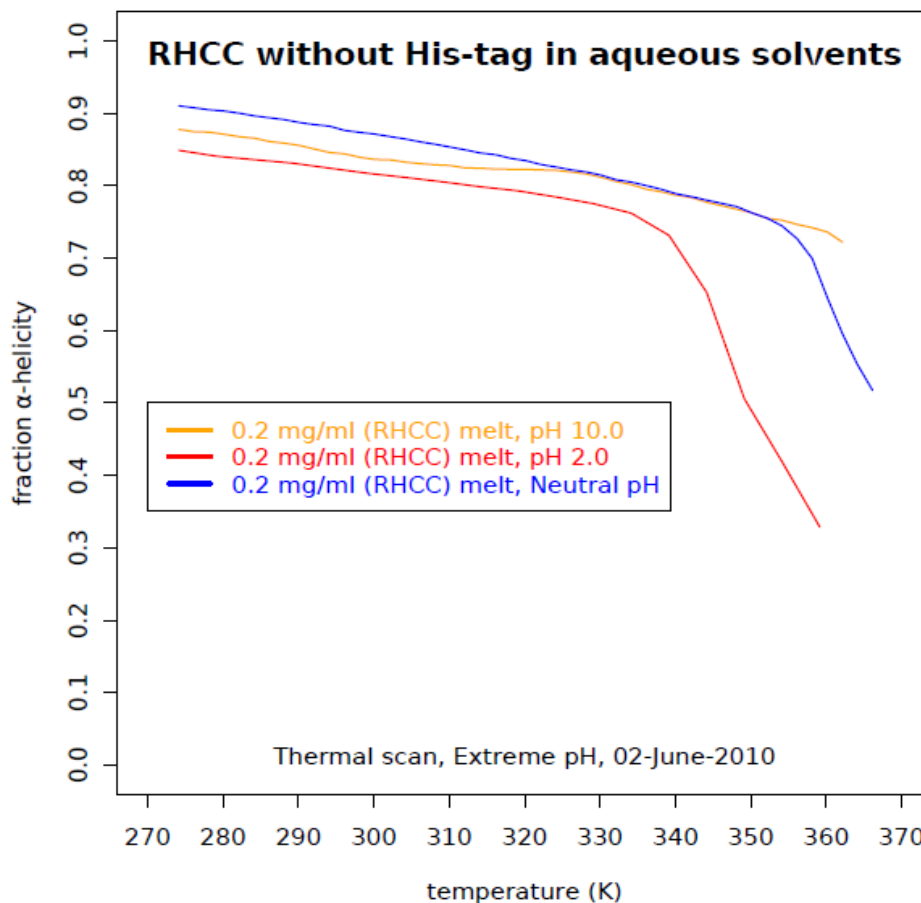


Figure 3-14: Thermal scan for fraction alpha helicity of RHCC measured at 222 nm. Temperature in Kelvin (x-axis1), fraction α -helicity. Temperature range of 1 to 93 was used and aqueous conditions at pH 2.0 (red), pH 7.0 (blue), pH 10.0 (orange) buffer.

Recently, Yuchi *et al.*, 2009 reported a chimeric, KcsA – RHCC channel. The aim of this study was to improve the thermal stability of the KcsA channel from *Streptomyces lividans* (Yuchi *et al.*, 2009). In this this current a fragment of RHCC was fused to the C-terminus of KcsA, which resulted in an increase in the melting temperature of KcsA from 36.9 °C to 78 °C at pH 4 and from 80.2 °C to >100 °C at pH 8.0, respectively. The RHCC fragment used by Yuchi comprised residues 16-52 which means that the first 15 residues are missing.

Interestingly, when Yuchi determined the melting temperature for the RHCC fragment (16-52) alone, the values obtained were 52 °C and 59 °C at pH 8 and pH 4 respectively. Taken together with the results presented here, it suggests that the N-terminal 15 residues of RHCC play a key role in the extreme thermostability of this 52 residue fragment of the tetrabrachion stalk.

3.4 Bioremediation of Mercury Hg^{2+} ions from aqueous solution

This section of our work investigates the potential of using RHCC as a novel bioremediator of mercury. For a long time, the mercury ion (Hg^{2+}) has been known to be extremely toxic due to its strong affinity of the thiol groups in proteins (Okino *et al.*, 2000). As a result it has the capability to accumulate overtime in biological organisms and the food chain (D'Itri 1972; Nriagu 1979; Saouter *et al.*, 1994). Indeed, mercury contamination both on the land and in the aquatic environments is a major concern worldwide due to the presence of mercury in industrial waste water (D'Itri 1972; Noyes *et al.*, 1976; Nriagu 1979). To date, investigations have shown that exposure to mercury has adverse effects on reproduction, the central nervous system, the liver, the kidney and finally that it causes sensory and psychological impairments. Significantly, it has been demonstrated that approximately two thirds of all mercury present in our natural environment are as a result of human activities as opposed to naturally occurring mercury (Rongjun *et al.*, 2009). But in order to tackle this problem it is necessary to understand the mechanism of mercury toxicity so that we can develop better strategies to limit the impact of mercury in the environment.

Mercury contamination poses a serious threat to our way of life. There are reports in the literature which describe physical (trapping and collecting) and chemical (precipitation, redox conversion) methods to separate and remove mercury from contaminated sites (Jones 1971; Noyes *et al.*, 1976). However, the effectiveness of these approaches is severely

compromised because they both cause secondary problems. For example, the physical approaches usually require additional treatments of the mercury waste, and with chemical mercury recovery methods they often leave hazardous by-products or residual sludges (Jo-Shu *et al.*, 1997). Thus, it is critical to search for new approaches, such as biological methods (bioremediation) that can trap different forms of mercury without the problems associated with these earlier methods. Previous biological methods developed in the field of mercury bioremediation have focused on the use of mercury resistant organisms that are capable of taking up and converting mercury to a less toxic form (Hansen *et al.*, 1984; Jo-Shu *et al.*, 1997; Sari & Tuzen, 2009).

In this study, the capability of RHCC to remove Hg^{2+} ions from an aqueous solution was investigated. The idea to use RHCC in mercury bioremediation comes from the fact that the cavities in the structure have an affinity for heavy metals (Stetefeld *et al.*, 2000). The research goal was therefore to determine if any type of mercury is capable of binding to RHCC. To test this hypothesis we used ionic mercury compounds such as mercury nitrate, $[\text{Hg}(\text{NO}_3)_2]$ and di-potassium mercury iodide $[\text{K}_2\text{HgI}_4]$, covalent mercury compounds like mercury bromide $[\text{HgBr}_2]$ and mercury chloride $[\text{HgCl}_2]$ or the alkylated mercury compounds like ethylmercury phosphate $[\text{C}_2\text{H}_7\text{HgO}_4\text{P}]$ and methyl-mercury chloride $[\text{CH}_3\text{HgCl}]$.

The ability of coiled-coil cavities to bind important heavy metals has been reported in the literature (Stetefeld *et al.*, 2000; Ozbek *et al.*, 2002; Eriksson *et al.*, 2009). We will introduce a preliminary novel approach, using RHCC cavities as a possible mercury (II) ion detoxifier from aqueous solutions. The biosorption mechanism of Hg^{2+} ions was probed at pH 7.5 (weakly alkaline). Mercury was detected using a Tekran mercury analyzer coupled to an atomic fluorescence detector, that has a sensitivity that extends down to parts per trillion. In addition, we also setup crystallization experiments of RHCC in the presence of these mercury

compounds to see if we can understand how Hg^{2+} is absorbed at the molecular level.

3.4.1 Solution analysis using dialysis and CVAFS detection method

3.4.1.1 Potassium Mercury Iodide (K_2HgI_4) analysis

Out of the three classes of mercury compounds used our results clearly show that RHCC is only capable of binding to mercury compounds such as mercury nitrate and iodide. No binding could be detected for the covalently bound or alkylated mercury compounds tested. In this experimental setup we are limited to measuring Hg(II) which is the reactive form of mercury found in the environment. The RHCC protein was unable to bind HgBr_2 , HgCl_2 , $\text{C}_2\text{H}_7\text{HgO}_4\text{P}$ and CH_3HgCl (data not shown). The covalent bond between mercury and the other atoms in all four compounds make the dissociation to form Hg^{2+} unlikely, hence the RHCC is unable to bind the mercury. Furthermore, the presence of the ethyl and methyl groups may cause steric effects that block the mercury from entering into the cavities. The data shows a rapid uptake of Hg^{2+} from mercury iodide within the first day (day 1) with a gradual increase over the next few days (Fig. 3-15). By keeping the protein concentration constant (0.1 mg/ml) and detecting the amount of Hg^{2+} that is taken up, we were able to determine the number of Hg^{2+} ions bound to RHCC (Sec. 3.4.1.3).

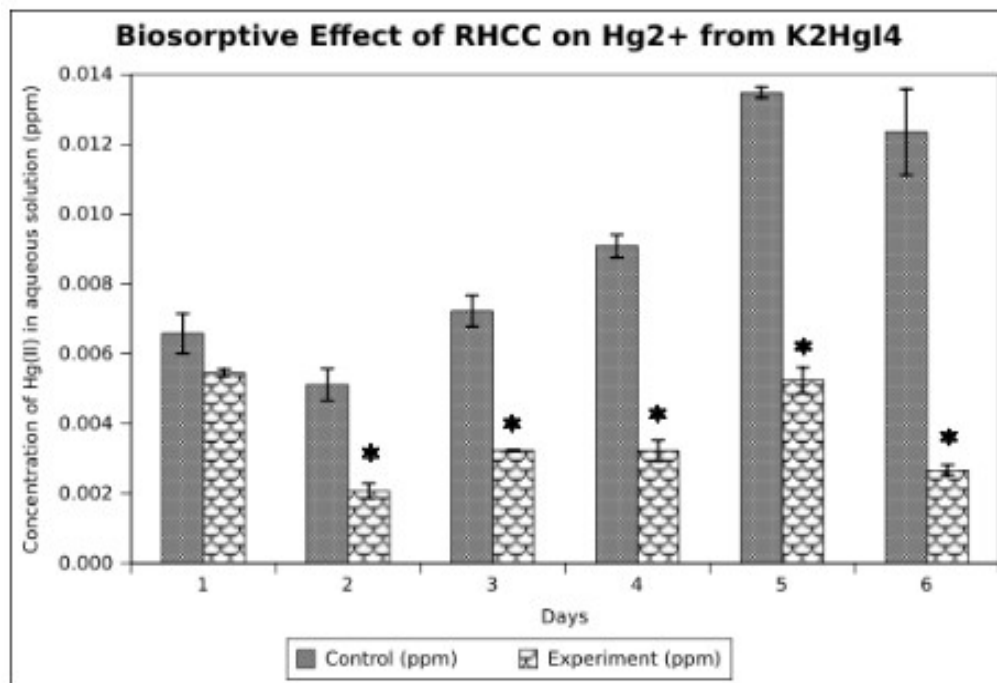


Figure 3-15: Uptake of Hg²⁺ ions by RHCC. Detection was by Cold Vapour Atomic Fluorescence Spectrometry. Column plot for Hg²⁺ ion concentration in the control and the absorption experiment was measured over a 6 day time period, n = 3 separate experiments. *P < 0.01 compared with control. The increased mercury concentration seen in the control is as a result of added mercury after each 24 hrs interval.

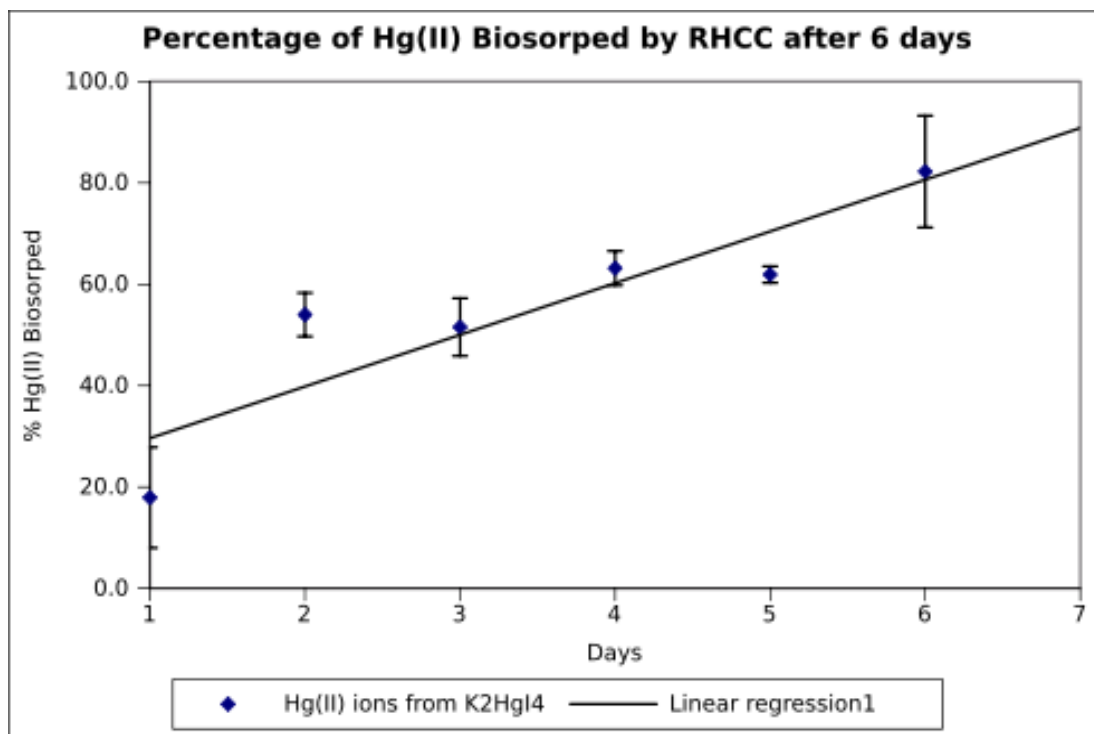


Figure 3-16: Biosorption of Hg^{2+} ion from potassium mercury iodide by RHCC. Experiments were performed over six in an aqueous buffer, pH 7.5.

Analysis of the data showed that RHCC absorbs approximately 20 % of the mercury from aqueous buffer within the first 24 hours, rising to approximately 80 % after 6 days (Fig. 3-16). As we will see later, X-ray diffraction analysis of the complex formed revealed that mercury ions were localized in the cavity of RHCC.

3.4.1.2 Mercury Nitrate ($\text{Hg}(\text{NO}_3)_2$) analysis

Experiments with mercury nitrate demonstrated that RHCC is able to bind higher amounts of Hg^{2+} (Fig. 3-17) than observed in the equivalent dipotassium mercury iodide

experiments. A possible explanation for this result is that the dissociation of mercury nitrate to its respective ions Hg^{2+} and NO_3^- means that RHCC is able to bind free Hg^{2+} without being sterically hindered or having to somehow break any covalent bond unlike the mercury iodide derivative.

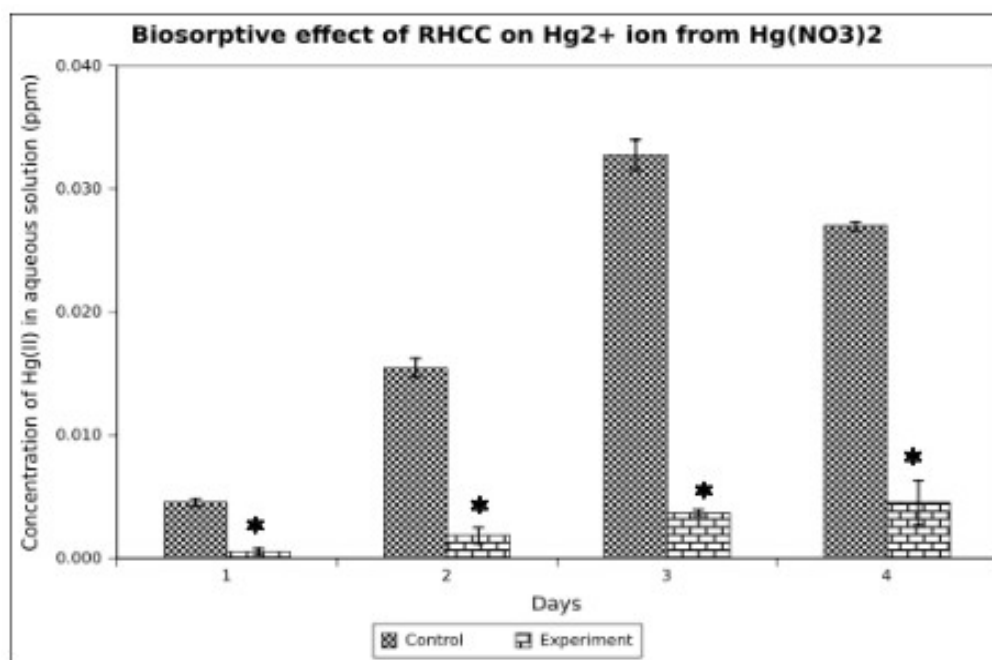


Figure 3-17: Effect of Hg^{2+} ions by RHCC. Detection was by Cold Vapour Atomic Fluorescence Spectrometry. (A) Column plot for Hg (II) ion concentration of control and experiment over a 4 day period. $n = 3$ separate experiments. $*P < 0.01$ compared with control. The increased mercury concentration seen in the control is as a result of added mercury after each 24 hrs interval.

In addition, we noticed a significant difference in the amount of mercury when comparing the control and the experiment after every incubation cycle. About 90 % of the Hg^{2+} ions were removed from the surrounding aqueous buffer by RHCC after 4 days which

compares with approximately 70 % for the mercury iodide experiment after 6 days. At longer incubation periods there was no additional uptake of Hg^{2+} ions by RHCC and even a slight decrease, which suggests that the binding capacity of RHCC has reached saturation level (Fig 3-18).

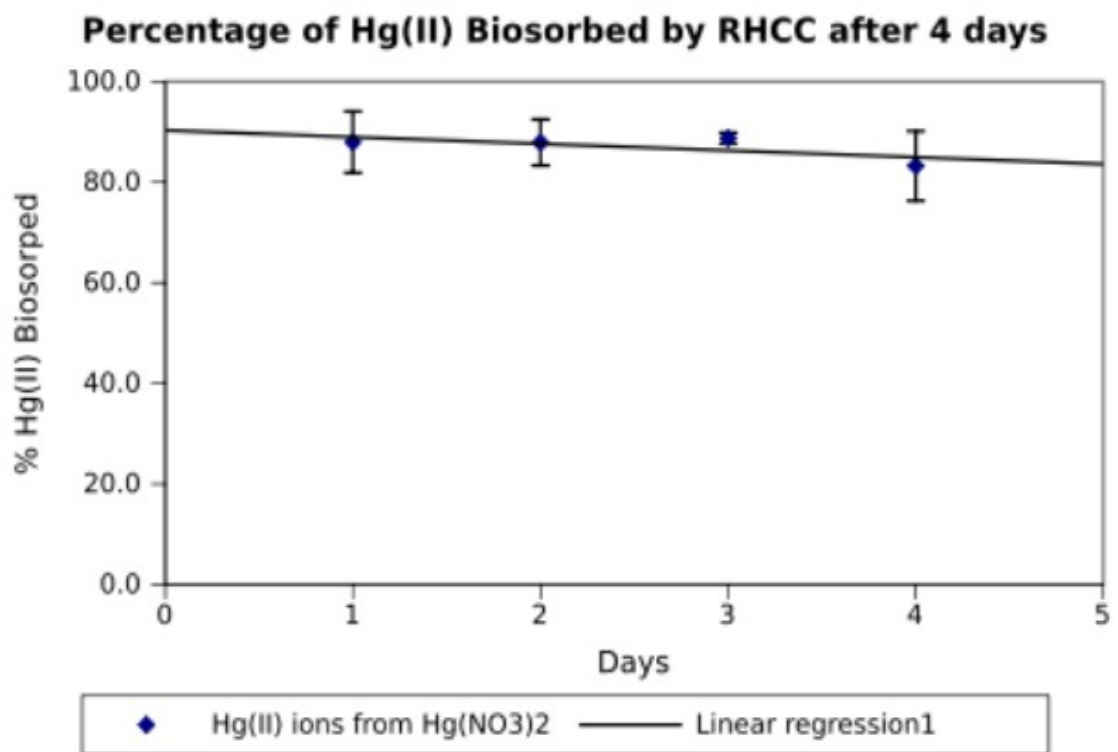


Figure 3-18: Biosorption of Hg^{2+} ion from mercury nitrate compound by RHCC.

Experiments were performed over four in an aqueous buffer, pH 7.5.

3.4.1.3 Determination of the ratio of Hg^{2+} bound to RHCC

We were also able to determine the number of Hg^{2+} ions that bind to RHCC (Fig. 3-19). This analysis showed that RHCC binds Hg^{2+} ions, more rapidly from mercury nitrate than from potassium mercury iodide. This may be explained in part by the fact that the nitrate

derivative was more soluble than the iodide derivative and so more Hg^{2+} is available to be absorbed by the RHCC. However this cannot be the whole story given the significant preference for mercury nitrate over Di-potassium mercury iodide.

Thus, we have demonstrated in principle that RHCC has a capacity to bind ionic mercury compounds such as mercury nitrate and Di-potassium mercury iodide. Instruments were tested for the presence of mercury prior to use, to exclude the possibility of mercury entering into the experiment from an external source. All mercury concentrations were determined in an Ultra-Clean Trace Element laboratory, by a specialized technician.

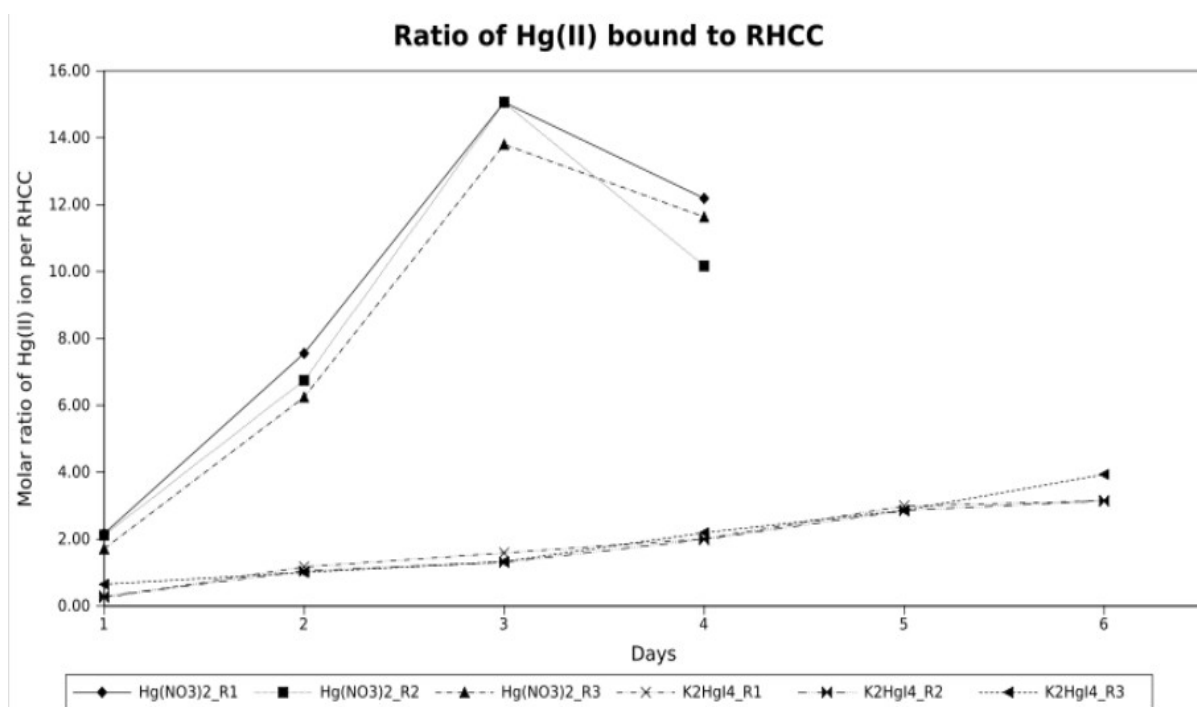


Figure 3-19: Line plot for the total number of Hg^{2+} bound to RHCC within a week. y-axis is the number of Hg(II) ion interacting with mercury and the x-axis shows the duration of time allowed for binding. All separate replicates are shown.

3.5 X-ray Crystallography analysis of Hg²⁺– RHCC complex

3.5.1 Non-thiol binding of Hg insight the hydrophobic cavities of RHCC

In the experimentally-phased electron density maps, 3 or 4 spheres of density were seen in the tetrameric core at cavities 2,3 and 4, respectively. Interestingly, anomalous signals for mercury could be detected only when K₂HgI₄ and Hg (NO₃)₂ were soaked into the crystals. This is a strong hint for the interaction between RHCC and the bivalent cation of Hg²⁺. Any other mercury derivatives were unable to be incorporated into the cavities. As shown in Figure 3-20, fully occupied electron clouds could be detected for the Hg, however, the other portions of the complex ions were not detectable in the X-ray crystallography experiments. Interestingly, mercury is not involved in the formation of hydrogen bonds between the CO-NH acceptor-donor system of the peptide backbone of the coiled-coil helices (Fig. 3-21). It seems to be that the mercury species inside the cavity is Hg⁰. This finding is very unusual and suggestive for a bimodal mechanism of interaction. In a first stage the bivalent cation is required to allow for the entering into the cavities. In a second stage the bivalent cation (Hg²⁺) has to be reduced and behaves like the elemental atom in the gas phase. Refinement statistics are summarized in Table 3-3.

An experimental proof for the first stage hypothesis is coming from superimpositions of different native and complexed RHCC structures (Fig. 3-22). We are convinced that the heavy atom diffuses through the electrostatic gates along the cavities, which is supported by major changes in the ionic and polar electrostatic interactions.

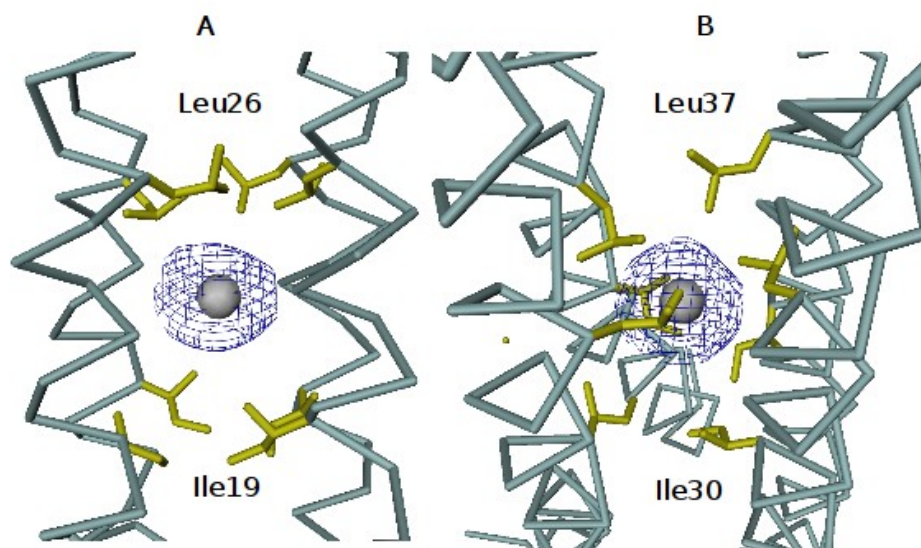


Figure 3-20: Anomalous difference Fourier map for mercury (K_2HgI_4 and $Hg(NO_3)_2$) insight the tetrameric channel of RHCC. The $C\alpha$ -backbone is shown in gray (render mode). The individual heavy atoms of mercury are drawn as gray spheres with the 4σ anomalous F_o-F_c map superimposed. Panel A and B are the second and third hydrophobic cavities from the N-terminal end. The hydrophobic side-chains are shown in yellow.

Table 3-3: Data collection and refinement statistics between RHCC at 1.4 Å (spacegroup P3₁21), 3.3 Å (spacegroup P2₁2₁2₁) and 3.15 Å (spacegroup P2₁2₁2₁) resolution measured in-house and in the Synchrotron. All data sets were measured at 100K.

Data collection statistics¹	Native	K ₂ HgI ₄	Hg(NO ₃) ₂
X-Ray source	in-house	Synchrotron	Synchrotron
	(1.5418Å)	(0.8472Å)	(0.8472Å)
Resolution (Å)	1.8 (1.49-1.40)	3.3 (3.48-3.3)	3.15 (3.5-3.15)
Observed reflections	104.333	79623	89769
Unique Reflections	46.100	7550	9025
Completeness	100.0 (96.6)	98.3 (94.4)	97.3 (96.4)
R _{sym} ²	6.5 (27.0)	8.4 (38.0)	7.4 (31.0)
Wilson B-factor (Å ²)	24.16	51.9	46.0
<I/σI>	11.6 (3.35)	8.3 (5.7)	10.3 (8.7)
Refinement statistics			
R _{factor} ³ (%), no sigma cutoff	23.1 (28.9)	24.8 (34.1)	26.3 (33.1)
R _{free} (%), no sigma cutoff	27.6 (29.9)	29.5 (38.3)	31.8 (36.7)
Mean B factor (Å ²)			
Protein atoms	18.8	37.86	37.86
Water molecules	41.3	68.9	68.9
Bonds (Å) ⁴	0.004	0.004	0.004
Angle (°) ⁴	0.7	0.72	0.72
Ramachandran Plot ⁵	100/ 0/ 0/ 0	100/ 0/ 0/ 0	100/ 0/ 0/ 0

¹Final shell in parenthesis. ²R_{sym} = $\sum |I - \langle I \rangle| / \sum I$. ³R_{factor} = $\sum |F_{obs} - |F_{calc}|| / \sum |F_{obs}|$. ⁴Root-mean-square error.

⁵Percentage of residues in most favoured/ additional allowed/ generously allowed and disallowed regions of the Ramachandran plot.

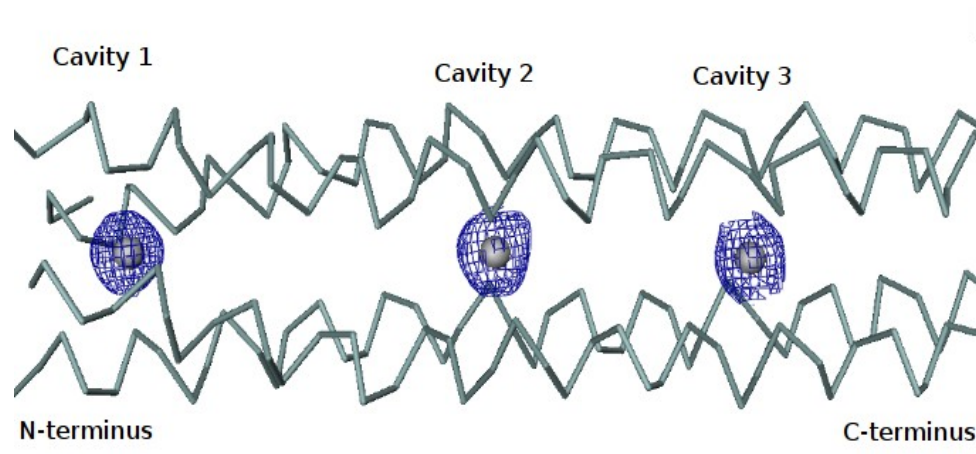


Figure 3-21: Detailed view of Superposition of the final refined 2DFo-mFc map (blue coloured) at 3.3.Å resolution (1.5 σ contour level) onto the crystal structure containing the Hg from the K₂HgI₄ soak experiment. Four helical segments (A-D) are shown as grey C α -traces in render mode. Individual Hg-atoms are shown as grey coloured spheres.

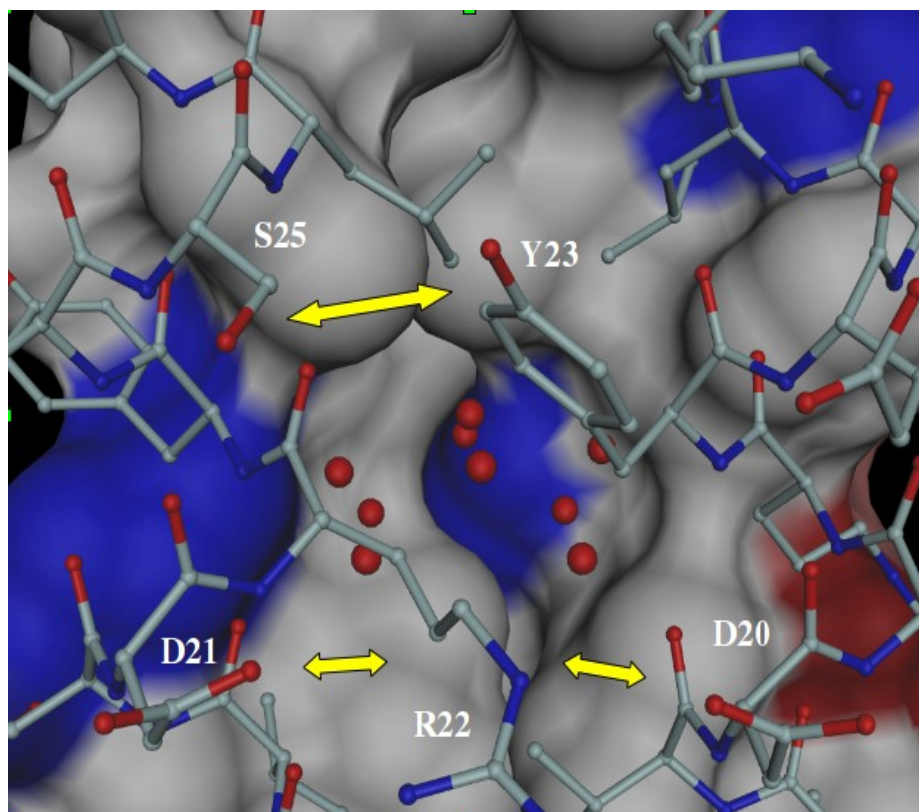


Figure 3-22. Structural changes upon mercury storage. Detailed view into the complex ionic network-surrounding cavity 2. Yellow arrows mark significant changes in essential amino acid sidechain configurations upon incorporation of the heavy atom derivatives. As well the Asp21-Arg22-Asp20 as the Tyr23-Ser25 interactions are modified.

4. Conclusions

In conclusion, the RHCC tetramer is a good example of how different interactions play pivotal role to confer extreme thermostability in protein. As mentioned earlier (Section 3.3), there is no single mechanism that is responsible for providing the stability we have observed in this hyperthermophilic protein. We have demonstrated that optimal hydrophobic packing in addition to an extended hydrophobic interhelical interface and a network of complex ionic salt-bridges possibly lead to a highly thermostable protein. With regards to the bioremediation of mercury by RHCC, our results show that positively charged mercury ions are easily taken up and localized within the cavity of the tetrabrachion suggesting that the protein can be used as a biological filter. Furthermore, the unique hydrophobic cavities of this coiled-coil protein have been applied in therapeutic drug delivery systems (Eriksson *et al.*, 2009). Considering the size of all four hydrophobic cavities researchers can develop a carrier pathfinder system for effective drug delivery.

It will be interesting to determine the rate of formation of RHCC-mercury complex, the effects of the solution pH on the binding affinity and the carrying capacity of RHCC, which will ultimately aide us to scale up the detoxification mechanism of RHCC. It will also be desirable to elucidate the mechanism by which RHCC binds to anticancer drugs so that we can develop a novel carrier pathfinder drug delivery system.

5. References

1. Woese, C.R. & Fox, G.E. (1977) Phylogenetic structure of the prokaryotic domain: The primary kingdoms. *Proc. Natl. Acad. Sci.* **74**: 5088-5090.
2. Woese, C.R. Magrum, L. J. & Fox, G.E. (1978) Archaeobacteria. *J. Mol. Evol.* **11**: 245-252.
3. Peters, J., Baumeister, W and Lupas, A. (1996) Hyperthermostable surface layer protein tetrabrachion from the archaeobacterium *Staphylothermus marinus*: evidence for the presence of a right-handed coiled coil derived from the primary structure. *Molecular Biology*, **257**: 1031-1041.
4. Mayr, J., Lupas, A., Kellermann, J., Eckerskorn, C., Baumeister, W. and Peters, J. (1996) A Hyperthermostable protease of the subtilisin family bound to the surface layer of the archaeon *Staphylothermus marinus*. *Curr. Biol.* **6**: 739-749.
5. Byun, J., Rhee, J, Kim, N.D, Yoon, J, Kim, D, Koh, E, Oh, J and Cho, H. (2007). Crystal structure of hyperthermophilic esterase EstE1 and the relationship between its dimerization and thermostability properties. *BMC Struct Biol*, **7**: 47.
6. Rhee, J., Kim, D, Ahn, D, Yun, J, Jang, S, Shin, H, Cho, H, Pan, J and Oh, J. (2006). Analysis of the thermostability determinants of hyperthermophilic esterase EstE1 based on its predicted three-dimensional structure. *Appl Environ Microbiol*, **72**: 3021-3025.
7. Vornrhein, C., Bönisch, H, Schäfer, G and Schulz, G.E. (1998). The structure of a trimeric archaeal adenylate kinase. *J Mol Biol*, **282**: 167-179.
8. Singleton, M., Isupov, M and Littlechild, J. (1999). X-ray structure of pyrrolidone carboxyl peptidase from the hyperthermophilic archaeon *Thermococcus litoralis*. *Structure*, **7**: 237-244.
9. Kirino, H., Aoki, M, Aoshima, M, Hayashi, Y, Ohba, M, Yamagishi, A, Wakagi, T and Oshima, T. (1994). Hydrophobic interaction at the subunit interface contributes to the thermostability of 3-isopropylmalate dehydrogenase from an extreme thermophile, *Thermus thermophilus*. *Eur J Biochem*, **220** :275-281.
10. Kelly, C.A., Nishiyama, M, Ohnishi, Y, Beppu, T and Birktoft, J.J. (1993). Determinants of protein thermostability observed in the 1.9-Å crystal structure of malate dehydrogenase from the thermophilic bacterium *Thermus flavus*. *Biochemistry*, **32**: 3913-3922.

11. Fiala, G., Stetter, K.O., Jannasch, H.W., Langworthy, T.A., Madon, J. (1986). *Staphylothermus marinus* sp. Nov. Represents a novel genus of extreme thermophilic submarine heterotrophic archaeobacteria growing up to 98°C. *System. Appl. Microbiol.* **8**: 106-113.
12. Wildhaber, I. and Baumeister, W. (1987). The cell envelope of *Thermoproteus tenax*: three-dimensional structure of the surface layer and its role in shape maintenance. *EMBO J*, **6**: 1475-1480.
13. Phipps, B.M., Hoffmann, A, Stetter, K.O and Baumeister, W. (1991). A novel ATPase complex selectively accumulated upon heat shock is a major cellular component of thermophilic archaeobacteria. *EMBO J*, **10**: 1711-1722.
14. Cohen, C., Parry, D.A.D., (1990) Alpha-helical coiled coils and bundles: how to design an alpha-helical protein. *Protein*. **7**: 1–15.
15. Walshaw, J. and Woolfson, D. N., (2001) SOCKET: a program for identifying and analysing coiled-coil motifs within protein structures. *J. Mol. Biol.* **307**: 1412-1450.
16. Perutz, M. F. (1951). *Rep. Prog. Chem.* **48**: 361-382.
17. Crick, F.H.C.. (1952). Is alpha-keratin a coiled coil?. *Nature*, **170**: 882-883.
18. Crick, F.H.C. (1953) *Acta Crystallogr.*, **6**: 689-697.
19. Wilson, I.A., Skehel, J.J and Wiley, D.C. (1981). Structure of the haemagglutinin membrane glycoprotein of influenza virus at 3 Å resolution. *Nature*, **289**: 366-373.
20. O'Shea, E.K., Klemm, J.D, Kim, P.S and Alber, T. (1991). X-ray structure of the GCN4 leucine zipper, a two-stranded, parallel coiled coil. *Science*, **254**: 539-544.
21. Efimov, V. P., Engel, J and , Malashkevich, V.N. (1996) Crystallization and preliminary crystallography study of the pentamerization domain from cartilage oligomeric matrix protein: a five-stranded alpha-helical bundle. *Protein*. **24**: 259-262.
22. Malashkevich, V.N., Kammerer, R.A., Efimov, V.P., Schulthess, T., Engel, J., (1996) The crystal structure of a five-stranded coiled coil in COMP: a prototype ion channel? *Science* **274**: 761–765.
23. Pauling, L., Corey, R. B. & Branson, H. R. (1951) The structure of proteins: two hydrogen-bonded helical configurations of the polypeptide chain. *Proc. Natl. Acad.*

- Sci USA*. **37**: 205–211.
24. Stetefeld, J., Jenny, M., Schulthess, T., Landwehr, R., Engel, J., Kammerer, R.A., (2000)
Crystal structure of a naturally occurring parallel right-handed coiled coil tetramer. *Nat. Struct. Biol.* **7**: 772–776.
25. Liu, J., Deng, Y., Zheng, Q., Cheng, C.S., Kallenbach, N.R., Lu, M., (2006) A seven-helix coiled coil. *Proc. Natl. Acad. Sci USA* **103**: 15457–15462.
26. Peters, J., Baumeister, W., Lupas, A., (1996) Hyperthermostable surface layer protein tetrabrachion from the archaebacterium *Staphylothermus marinus*: evidence for the presence of a right-handed coiled coil derived from the primary structure. *J. Mol. Biol.* **257**: 1031–1041.
27. Kühnel, K., Jarchau, T., Wolf, E., Schlichting, I., Walter, U., Wittinghofer, A., Strelkov, S.V., (2004) The VASP tetramerization domain is a right-handed coiled coil based on a 15-residue repeat. *Proc. Natl. Acad. Sci. U.S.A.* **101**: 17027–17032.
28. Hoiczky, E., Roggenkamp, A., Reichenbecher, M., Lupas, A., Heesemann, J., (2000) Structure and sequence analysis of *Yersinia* YadA and *Moraxella* UspAs reveal a novel class of adhesins. *EMBO J.* **19**: 5989–5999.
29. Nooren, I.M.A., Kaptein, R., Sauer, R.T., Boelens, R., (1999) The tetramerization domain of the Mnt repressor consists of two right-handed coiled coils. *Nat. Struct. Biol.* **6**: 755–759.
30. Tarbouriech, N., Curran, J., Ruigrok, R.W.H., Burmeister, W.P., (2000) Tetrameric coiled-coil domain of Sendai virus phosphoprotein. *Nat. Struct. Biol.* **7**: 777–781.
31. Harbury, P.B., Plecs, J.J., Tidor, B., Alber, T and Kim, P.S. (1998). High-resolution protein design with backbone freedom. *Science*, **282**: 1462-1467.
32. Litowski, J.R., Hodges, R.S., 2001. Designing heterodimeric two-stranded alpha-helical coiled-coils: the effect of chain length on protein folding, stability and specificity. *J. Pept. Res.* **58**: 477–492.
33. Fairman, R., Chao, H., Mueller, L., Lavoie, T.B., Shen, L., Novotny, J., Matsueda, G.R. (1995). Characterization of a new four-chain coiled-coil: Influence of chain length on stability. *Protein Sci.* **4**: 1457-1469.
34. Su, J.Y., Hodges, R.S and Kay, C.M. (1994). Effect of chain length on the

- formation and stability of synthetic alpha-helical coiled coils. *Biochemistry*, **33**: 15501-15510.
35. Lumb, K.J., Carr, C.M and Kim, P.S. (1994). Subdomain folding of the coiled coil leucine zipper from the bZIP transcriptional activator GCN4. *Biochemistry*, **33**: 7361-7367.
36. Munson, M., Balasubramanian, S., Fleming, K.G., Nagi, A.D., O'Brien, R., Sturtevant, J.M. , Regan, L. (1996) What makes a protein a protein? Hydrophobic core design that specify stability and structural properties. *Prot. Sci.* **5**: 1584-1593.
37. Lavigne, P., Sönnichsen, F.D, Kay, C.M and Hodges, R.S. (1996). Interhelical salt bridges, coiled-coil stability, and specificity of dimerization. *Science*, **271**: 1136-1138.
38. McClain, D.L., Gurnon, D.G and Oakley, M.G. (2002). Importance of potential interhelical salt-bridges involving interior residues for coiled-coil stability and quaternary structure. *J Mol Biol*, **324**: 257-270.
39. Meier, M., Lustig, A, Aebi, U and Burkhard, P. (2002). Removing an interhelical salt bridge abolishes coiled-coil formation in a de novo designed peptide. *J Struct Biol*, **137**: 65-72.
40. Meier, M., Stetefeld, J., Burkhard, P., (2010) The many types of interhelical ionic interaction in coiled coils-An Overview. *Structural Biology*. **2**: 192-201.
41. Ladenstein, R., Antranikian, G. (1998) Proteins from hyperthermophiles: Stability and enzymatic catalysis close to the boiling point of water. *Advances in Biochemical Engineering/Biotechnology*. **61**: 37-85.
42. Peters, J., Nitsch, M., Kühlmorgen, B., Golbik, R., Lupas, A., Kellermann, J., *et al.*, (1995) Tetrabrachion: a filamentous archaeobacterial surface protein assembly of unusual structure and extreme stability. *Molecular Biology*, **245**: 385-401.
43. Chou, C., Jenney, F.E.J, Adams, M.W.W and Kelly, R.M. (2008). Hydrogenesis in hyperthermophilic microorganisms: implications for biofuels. *Metab Eng*, **10**: 394-404.
44. Scandurra, R., Consalvi, V., Chiaraluce, R., Politi, L., Engel, P.C. (1998) Protein thermostability in extremophiles. *Biochemistry*, **80**: 933-941.
45. Tripet, B., Wagschal, K, Lavigne, P, Mant, C.T and Hodges, R.S. (2000). Effects of

- side-chain characteristics on stability and oligomerization state of a de novo-designed model coiled-coil: 20 amino acid substitutions in position "d". *J Mol Biol*, **300**: 377-402.
46. Wagschal, K., Tripet, B, Lavigne, P, Mant, C and Hodges, R.S. (1999). The role of position a in determining the stability and oligomerization state of alpha-helical coiled coils: 20 amino acid stability coefficients in the hydrophobic core of proteins. *Protein Sci*, **8**: 2312-2329.
 47. Stellwagen, E. and Wilgus, H. (1978). Relationship of protein thermostability to accessible surface area. *Nature*, **275**: 342-343.
 48. Kammerer, R. A ., Schulthess, T ., Landwehr, R ., Lustig, A ., Fischer, D., Engel, J. (1998) Tenascin-C hexabrachion assembly is a sequential two-step process initiated by coiled-coil alpha-helices. *Biological Chemistry*. **273**: 10602-10608.
 49. McFarlane, A. A., Orriss, G., Stetefeld, J. (2009) Review - The use of coiled coil proteins in drug delivery systems. *Eur. J. of Phar.* **625**: 101-107.
 50. Matthew, B. W., and Liu, L. (2009) A review about nothing: Are apolar cavities in proteins really empty? *Prot. Sci.* **18**: 494-502.
 51. Rashin, A. A., Iofin, M., and Honig, B. (1986) Internal cavities and buried waters in globular proteins. *Biochem.* **25**: 3619-3625.
 52. Williams, M. A., Goodfellow, J. M., and Thornton, J. M. (1994) Buried waters and internal cavities in monomeric proteins. *Prot. Sci.* **3**: 1224-1235.
 53. Buckle, A. M., Cramer, P., and Fersht, A. R. (1996) Structural and energetic responses to cavity-creating mutations in hydrophobic cores: observation of a buried water molecule and the hydrophilic nature of such hydrophobic cavities. *Biochem.* **35**: 4298-4305.
 54. Liu, L., Baase, W. A., Micheal, M. M., and Matthews, B. W. (2009) Use of stabilization mutation to engineer a charged group with a ligand binding hydrophobic cavity in T4 lysozyme. *Biochem.* **48**: 8842-8851.
 55. Özbek, S., Engel, J., and Stetefeld, J. (2002) Storage function of cartilage oligomeric matrix protein: the crystal structure of the coiled-coil domain in complex with vitamin D3. **21**: 5960-5968.
 56. Gonzalez-Fernandez, F., Bevilacqua, T., Lee, K., Chandrashekar, R. *et al.*, (2009)

- Retinol-binding site in interphotoreceptor retinoid-binding protein (IRBP): A novel hydrophobic cavity. *IOVS*. **50**: 5577-5586.
57. Mizuno, T., Hasegawa, C., Tanabe, Y., Hamajima, K., Muto, T., *et al.*, (2009) Organic ligand binding by a hydrophobic cavity in a designed tetrameric coiled-coil Protein. *Chem. Eur. J.* **15**: 1491-1498.
 58. Gonzalez, L., Jr., Plecs, J. J., Alber, T. (1996). An engineered allosteric switch in Leucine-zipper oligomerization. *Nat. Struct. Biol.* **3**: 510 –515
 59. Hansen, C. L., Zwolinski, G., Martin, G., and Williams, J. W. (1984) Bacterial mercury removal from sewage. *Biotech. Bioeng.* **26**: 1330-1333.
 60. Ku, Y., Wu, M and Shen, Y. (2002) Mercury removal from aqueous solution by zinc cementation. *Waste Management.* **22**: 712-726
 61. Kostal, J., Mulchandani, A., Groop, K. E and Chen, W. (2003) A temperature responsive biopolymer for mercury remediation. *Environ. Sci. Technol.* **37**: 4457-4462.
 62. Porath, J., Carlsson, J, Olsson, I and Belfrage, G. (1975). Metal chelate affinity chromatography, a new approach to protein fractionation. *Nature*, **258**: 598-599.
 63. Studier, F.W., Rosenberg, A.H, Dunn, J.J and Dubendorff, J.W. (1990). Use of T7 RNA polymerase to direct expression of cloned genes. *Methods Enzymol*, **185**: 60-89.
 64. Schägger, H. and von Jagow, G. (1987). Tricine-sodium dodecyl sulfate-polyacrylamide gel electrophoresis for the separation of proteins in the range from 1 to 100 kDa. *Anal Biochem*, **166**: 368-379.
 65. Schägger, H. (2006). Tricine-SDS-PAGE. *Nat Protoc*, **1**: 16-22.
 66. Cantor, C.R., and Schimmel P.R. (1980). Size and shape of macromolecules. *In* Biophysical Chemistry, Part II: Techniques for the Study of Biological Structure and Function. McCombs L.W., editor. Freeman W.H., and company, New York. 539-590.
 67. Laue, T.M., Shah, B.D., Ridgeway, T.M., Pelletier, S.L. (1992). Computer-aided interpretation of analytical sedimentation data for proteins, in: Harding, S.E., Rowe, A.J., Horton, J.C. (Eds.), *Analytical Ultracentrifugation in Biochemistry and Polymer Science*. Royal Society of Chemistry, Cambridge, United Kingdom, pp.

90-125.

68. Leslie, A.G.W. (1994). MOSFILM Users Guide, *Medical Research Council-Laboratory of Molecular Biology*, Cambridge, UK.
69. DeLano, W.L. and Brünger, A.T. (1994). Helix packing in proteins: prediction and energetic analysis of dimeric, trimeric, and tetrameric GCN4 coiled coil structures. *Proteins*, **20**: 105-123.
70. CCP4. (1994). The CCP4 Suite: Programs for Protein Crystallography. *Acta Cryst. D50*, 760- 763.
71. Brünger, A.T., Adams, P.D, Clore, G.M, DeLano, W.L, Gros, P, Grosse-Kunstleve, R.W, Jiang, J.S, Kuszewski, J, Nilges, M, Pannu, N.S, Read, R.J, Rice, L.M, Simonson, T and Warren, G.L. (1998). Crystallography & NMR system: A new software suite for macromolecular structure determination. *Acta Crystallogr D Biol Crystallogr*, **54**, 905-921.
72. Turk,D. (1992) Further development of a program for molecule graphic arts and electron density manipulation and its application to different protein-structure analysis. PhD Thesis, Technical University, Munich.
73. Greenfield, N.J. (2006). Using circular dichroism spectra to estimate protein secondary structure. *Nat Protoc*, **1**: 2876-2890.
74. Taylor, J. W. & Kaiser, E. T. (1987). Structure–function analysis of proteins through the design, synthesis, and study of peptide models. *Methods Enzymol.* **154**: 473–498.
75. Scandurra, R., Consalvi, V., Chiaraluce, R., Politi, L., Engel, P.C. (1998) Protein thermostability in extremophiles. *Biochem.* **80**: 933-941.
76. Perutz M.F., Raidt H. (1975) Stereochemical basis of heat stability in bacterial ferredoxins and in hemoglobin A2. *Nature* **225**: 255-259.
77. Perutz, M.F. (1978) Electrostatic effects in proteins. *Science*, **210**: 1187-1191.
78. Delboni L.F., Mande S.C., Rentier-Delrue F., Mainfroid V., Turley S., Vellieux F.M.D., Martial J.A., Hol W.G.J. (1995) Crystal structure of recombinant triphosphate isomerase from *Bacillus stearothermophilus*. An analysis of potential thermostability factors in six isomerases with known three dimensional structures points to the importance of hydrophobic interactions. *Protein Sci.* **4**: 2594-2604.

79. Hendsch Z.S., Tidor B. (1994) Do salt bridges stabilize proteins? A continuum electrostatic analysis. *Prot. Sci.* **3**: 1144-1149.
80. Honig, B. and Nicholls, A. (1995). Classical electrostatics in biology and chemistry. *Science*, **268**: 1144-1149.
81. Harbury, P.B., Zhang, T, Kim, P.S and Alber, T. (1993). A switch between two-, three-, and four-stranded coiled coils in GCN4 leucine zipper mutants. *Science*, **262**: 1401-1407.
82. Malashkevich, V.N., Kammerer, R.A, Efimov, V.P, Schulthess, T and Engel, J. (1996). The crystal structure of a five-stranded coiled coil in COMP: a prototype ion channel?. *Science*, **274**: 761-765.
83. Greenfield, N. J. (2004). Analysis of circular dichroism data. *Methods Enzymol.* **383**, 282–317.
84. Marquardt, D. W. (1963). An algorithm for leastsquares estimation of nonlinear parameters. *J. Soc. Ind. Appl. Math.* **11**: 431–441.
85. Shohei Okino, Kazuhiro Iwasaki, Osami Yagi & Hideo Tanaka. 2000. Development of a biological mercury removal-recovery system. *Biotechnology Letters*, **22**: 783-788.
86. D'Itri, F. M. (ed.) (1972). The environmental mercury problem. CRC Press Cleveland, OH.
87. Saouter, E., Turner R., Barkay, T. (1994). Microbial reduction of ionic mercury for the removal of mercury form contaminated environments. *Ann. NY Acad. Sci.* **721**: 423-427.
88. Noyes, O.R., Handy, M. K., Muse, L. A. J. (1976). Control of mercury pollution. *Toxicol. Environ. Health* **1**: 409-420.
89. Nriagu, J. O.(ed.) (1979). Biogeochemistry of mercury in the environment Elsevier/North-Holland Biochemical Press, New York.
90. Rongjun Q., Changmei S., Fang M., Ying Z., Chunnuan J., Qiang X., Chunhua W., Hou C. (2009). *Journal of Hazardous Materials* **167**: 717-727.
91. Jones, H. R. (ed.) (1971). Mercury pollution control. Noyes Data Corp., Park Ridge, NJ.
92. Chang, J., Law, W. (1997). Development of microbial mercury detoxification

- processes using mercury-hyperresistant strain of *Pseudomonas aeruginosa* PU21. *Biotechnol and Bioeng.* **57**: 4.
93. Hansen, C. L., Zwolinski, G., Martin, D., Williams, J. W. (1984). Bacterial removal of mercury from sewage. *Biotechnol. Bioeng.*, **26**: 1330-1333.
94. Sari, A., Tuzen, M. 2009. Removal of mercury (II) from aqueous solution using moss (*Drepanocladus revolvens*) biomass: Equilibrium, thermodynamic and kinetics studies. **171**: 500-507.
95. Method 1631, Revision E: Mercury in Water by Oxidation, Purge and Trap, and Cold Vapour Atomic Fluorescence Spectrometry.
96. Kishan, K.V., Newcomer, M.E, Rhodes, T.H and Guillot, S.D. (2001). Effect of pH and salt bridges on structural assembly: molecular structures of the monomer and intertwined dimer of the Eps8 SH3 domain. *Protein Sci*, **10**, 1046-1055.
97. Wiegel, J.. (1998). Anaerobic alkalithermophiles, a novel group of extremophiles. *Extremophiles*, **2**, 257-267.
98. Yuchi, Z., Pau, V.P.T, Lu, B.X, Junop, M and Yang, D.S.C. (2009). An engineered right-handed coiled coil domain imparts extreme thermostability to the KcsA channel. *FEBS J*, **276**: 6236-6246.
99. Harrison, S.C.. (2004). Whither structural biology?. *Nat Struct Mol Biol*, **11**: 12-15.